Taylor & Francis
Taylor & Francis Group

Combustion Science and Technology

ISSN: (Print) (Online) Journal homepage: https://www.tandfonline.com/loi/gcst20

A Maximum Entropy-Inspired Interpolative Closure for the Prediction of Radiative Heat Transfer in Laminar Co-Flow Diffusion Flames

J. A. R. Sarr, C. P. T. Groth & J. C. T. Hu

To cite this article: J. A. R. Sarr, C. P. T. Groth & J. C. T. Hu (2022) A Maximum Entropy-Inspired Interpolative Closure for the Prediction of Radiative Heat Transfer in Laminar Co-Flow Diffusion Flames, Combustion Science and Technology, 194:1, 45-79, DOI: 10.1080/00102202.2019.1678376

To link to this article: https://doi.org/10.1080/00102202.2019.1678376

COMBUSTION SCIENCE AND TECHNOLOGY
2022, VOL. 194, NO. 1, 45–79
https://doi.org/10.1080/00102202.2019.1678376

Taylor & Francis
Taylor & Francis Group

A Maximum Entropy-Inspired Interpolative Closure for the Prediction of Radiative Heat Transfer in Laminar Co-Flow Diffusion Flames

J. A. R. Sarr[a], C. P. T. Groth[a], and J. C. T. Hu[b]

[a]Institute for Aerospace Studies, University of Toronto, Toronto, Ontario, Canada; [b]Pratt & Whitney Canada (P&WC), Mississauga, Ontario, Canada

ABSTRACT

An interpolative-based first-order maximum entropy (M_1) moment closure for providing approximate solutions to the equation of radiative transfer in non-gray participating media is proposed and described. This newly developed non-gray moment closure technique results in significant computational savings compared to an approach that makes use of the direct numerical solution of the optimization problem for entropy maximization. Its predictive capabilities are also assessed by comparing its solutions to those of the more commonly adopted first-order spherical harmonics (P_1) moment closure technique, as well as the popular discrete ordinates method (DOM), which is used as a benchmark for the model comparisons. The evaluations are performed for sooting co-flow laminar diffusion flames for blends of ethanol and methane fuels at atmospheric as well as at elevated pressures and include comparisons to available experimental data for soot volume fraction and flame temperature. The strong spectral dependence exhibited by the absorption coefficient of real gases is treated herein using the statistical narrow-band correlated-*k* method, and the chemical kinetics of the underlying species are modeled using a reduced mechanism for methane and ethanol fuels. Theoretical details of the proposed interpolative M_1, along with a description of the proposed Godunov-type finite-volume scheme developed for the numerical solution of the resulting system of hyperbolic moment equations are briefly discussed. The finite-volume method makes use of limited second-order solution reconstruction, multi-block body-fitted quadrilateral meshes with anisotropic adaptive mesh refinement (AMR), and an efficient Newton–Krylov–Schwarz (NKS) iterative method for solution of the resulting nonlinear algebraic equations arising from the finite-volume discretization procedure. The numerical results for laminar co-flow flames show that the flame solutions and predictions of soot formation of the non-gray M_1 maximum-entropy moment closure are very promising and in very good agreement with those of both the DOM and P_1 spherical harmonics model, while offering a substantial reduction in the number of dependent solution variables, compared to the DOM.

ARTICLE HISTORY
Received 19 January 2019
Revised 1 October 2019
Accepted 2 October 2019

KEYWORDS
Laminar diffusion flames; radiative heat transfer; moment closures; maximum entropy; optimization; efficiency

Introduction and motivation

Energy production and transportation systems in today's society still rely heavily on the combustion of hydrocarbons. However, this process is generally incomplete, thereby

CONTACT J. A. R. Sarr joachimandre.sarr@mail.utoronto.ca University of Toronto Institute for Aerospace Studies, 4925 Dufferin Street, Toronto, OntarioM3H 5T6, Canada

Color versions of one or more of the figures in the article can be found online at www.tandfonline.com/gcst.

producing unburnt products, such as very small-sized carbonaceous particulate matter (PM) or soot. The latter has been identified as a serious health hazard, on top of being an important factor of global warming and air pollution (Perera 2016). In an effort to develop more efficient and environmentally friendly combustion devices for transportation systems as well as industrial energy production, significant effort has been directed toward understanding the formation of combustion generated particles.

In order to obtain accurate predictions of pollutants such as soot at realistic engine operating conditions, a consistent combustion model must include all the relevant underlying phenomena such as fluid flow, chemical kinetics, heat and mass transfer, turbulence. Among the three different modes of heat transfer, namely conduction, convection and radiation, the latter can be dominant in flames due to its strong dependence on temperature. As such, accurate radiation modeling is therefore required in order to obtain accurate predictions of soot in combustion devices.

The transport of radiation in a participating media is governed by the radiative transfer equation (RTE) (Modest 2013). The latter is a complex integro-differential equation with high dimensionality, since the distribution of radiation is a function of seven independent variables. There exists no general analytical solution to the RTE, and approximate numerical solution procedures are generally sought.

The discrete ordinates method (DOM) (Fiveland 1984) is one of the most widely used models for providing approximate solutions of the RTE. Solutions of the DOM are generally obtained using space marching techniques, which are known to be very efficient for problems with relatively simple geometry and simplified physics (e.g., non-scattering media). However, space marching techniques can lose their effectiveness in cases with complex geometries and realistic physics (Charest, Groth, Gülder 2012), as is the case in many practical applications. The method of moments (Grad 1949) provides a hierarchy of models allowing a possible reduction in the numerical costs associated with solving the RTE. Such an approach replaces the representation of the angular dependence of the radiative distribution by a finite set of angular integrals or moments of the latter. However, closure is required for moment models since there are more unknowns than equations. The spherical harmonics approximation (P_N, where N refers to the order of the approximation), in particular the P_1 approximation, has been extensively used to model radiation heat transfer in combustion systems (Gupta, Modest, Haworth 2009; Li and Modest 2003; Mazumder and Modest 1999; Modest and Mehta 2006), but is generally only accurate in media with near-isotropic distribution. More recently, maximum-entropy-based closures (Dubroca and Feugeas 1999) have received particular attention in the field of radiation modeling due to their ability to accurately capture a wide range of optical conditions (both equilibrium and non-equilibrium regimes). Moreover, they have many desirable properties and take the most likely form of the distribution among all the possible ones for a given finite set of moments (Jaynes 1957). However, unlike the P_N moment closures for which analytic expressions for the closure relation exist for any order of approximation, N, for the M_N closures, analytic expression for the closure relation only exists for the gray M_1 closure, and, as such, the corresponding optimization problem for entropy maximization must be solved numerically, whenever an update of the radiation solution is required for higher-order closures and/or non-gray applications. In order to take advantage of the desirable properties of the M_N closures, an efficient alternative to the prohibitive

computational costs associated with the repeated solution of the optimization problem for entropy maximization is needed.

A tabulated, multigroup, non-gray M_1 closure was developed previously by Turpault (2002, 2005). In this approach, the Eddington factor, which is the only unknown in the Eddington tensor, was evaluated numerically by solving the optimization problem for entropy maximization for given sets of band-averaged angular moments. As mentioned previously, the repeated solution of the optimization problem for entropy maximization is however undesirable, since it can be prohibitively expensive for practical computations. In the context of reactive flows in either laminar or turbulent regimes, where the radiative properties of reacting gases, in particular the absorption coefficients of carbon dioxide (CO_2), water vapor (H_2O), and carbon monoxide (CO) strongly depend on wavenumber, such an approach would be prohibitively expensive, even with the current state-of-the-art spectral techniques (Liu, Smallwood, & Gülder, 2000a; Modest and Zhang 2002) for radiation calculations in non-gray participating media.

More recently, Pichard et al. (2016) developed an analytical approximation of the M_1 closure relation in the case of the Bolztmann entropy, based on pre-computed solutions of the optimization problem for entropy maximization, by writing the Eddington factor as a convex combination of its known exact analytical expressions on the boundaries of the realizability domain for moments up to first order. Additionally, in other previous work, Sarr, Groth, Hu (2019) developed a realizable and hyperbolic interpolative-based analytical approximation of the non-gray M_1 closure in the case of the entropy of radiation based on Bose-Einstein statistics. The latter is based on an approximation of the Eddington factor as a convex combination of its known exact analytic expressions in the isotropic and the free-streaming limits, and approximates pre-computed solutions of the optimization problem for entropy maximization. The implementation of this interpolative-based M_1 closure in the context of existing state-of-the-art spectral techniques, in particular the statistical narrow-band correlated-*k* (SNBCK) model, was also considered and its predictive capabilities were examined for several tests problems involving radiative heat transfer between parallel plates and within rectangular enclosures. For all the cases considered by Sarr, Groth, Hu (2019), the newly developed interpolative-based M_1 closure was observed to provide more accurate solutions than the P_1 closure while also providing extra computational robustness and incurring only a rather modest or minor increase in computational costs relative to the P_1 closure.

While both the discrete ordinates method and the spherical harmonics moment closures have been extensively used to provide approximate radiation solutions in numerical simulations of reactive flows (Gupta, Modest, Haworth 2009; Li and Modest 2003; Mazumder and Modest 1999; Modest and Mehta 2006), whether laminar or turbulent, to the authors knowledge, there has not been any previous studies related to the direct application of non-gray maximum entropy moment closures to reactive flows simulation. In this study, the assessment of the predictive capabilities of the newly developed non-gray M_1 closure of Sarr, Groth, Hu (2019) is extended to the case of laminar reacting flows. More specifically, the interpolative-based M_1 closure is used in the computational framework developed by Charest, Groth, Gülder (2010) for predicting laminar reactive flows with soot formation in various methane-air and ethanol-methane-air flames. The steady-state solutions of laminar co-flow diffusion flames obtained using the different radiation models, i.e., the M_1 and P_1 moment closures and the DOM, are then compared.

The SNBCK method was again used to quantify gas band absorption. At present, a rather simple semi-empirical two-equation model is used to predict the nucleation, growth, and oxidation of soot particles. The framework is applied to two laminar co-flow diffusion flames which were previously studied numerically and experimentally. Both a sooting methane-air flame and a sooting ethanol-methane-air flame are considered for validation purposes. Numerical predictions for these flames are verified with published experimental results. The newly developed M_1 closure was observed to yield reasonable agreement with experimental measurements for both flames for predictions of flame height, temperature and soot volume fraction.

Governing equations

Gas-phase multicomponent combusting flows can generally be described by a set of equations consisting of the conservation of total mass, individual species mass, mixture momentum, and mixture (Charest, Groth, Gülder 2010; Kuo 2005). In addition to those conservation equations, modeling soot formation and destruction in gaseous combustion also requires tracking an additional solid phase and capturing the interactions that occur between phases. The approach used in this work is similar to the empirical models developed by Leung, Lindstedt, and Jones (1991) and Fairweather, Jones, and Lindstedt (1992). In this approach, the soot particle size distribution is approximated by an average size that varied via surface reactions and coagulation, the representation of which requires only two additional transport equations for soot mass and number.

The conservation of global mass, momentum, energy, individual species mass, soot mass, and particle number, under the assumption of a Newtonian flow, can be summarized as

$$\frac{\partial \rho}{\partial t} + \nabla \cdot (\rho \mathbf{v}) = 0 \tag{1}$$

$$\frac{\partial}{\partial t}(\rho \mathbf{v}) + \nabla \cdot (\rho \mathbf{v}\mathbf{v} + p\mathbf{I}) = \nabla \cdot \tau + \rho \mathbf{g} \tag{2}$$

$$\frac{\partial}{\partial t}(\rho e) + \nabla \cdot \left[\rho \mathbf{v}\left(e + \frac{p}{\rho}\right)\right] = \nabla \cdot (\mathbf{v} \cdot \tau) - \nabla \cdot \mathbf{q} + \rho \mathbf{g} \cdot \mathbf{v} \tag{3}$$

$$\frac{\partial}{\partial t}(\rho Y_k) + \nabla \cdot [\rho Y_k(\mathbf{v} + \mathbf{V}_k)] = \dot{\omega}_k, \quad k = 1, \ldots, N \tag{4}$$

$$\frac{\partial}{\partial t}(\rho Y_s) + \nabla \cdot [\rho Y_s(\mathbf{v} + \mathbf{V}_Y)] = S_Y \tag{5}$$

$$\frac{\partial}{\partial t}(\rho N_s) + \nabla \cdot [\rho N_s(\mathbf{v} + \mathbf{V}_N)] = S_N \tag{6}$$

where t is the time, ρ is the mixture density, p is the total mixture pressure, $\mathbf{v}$ is the mixture velocity vector, e is the total mixture energy, Y_k is the mass fraction of species k, Y_s is the mass fraction of soot, N_s is the soot number density (number of particles per unit mass of mixture), $\mathbf{V}_k$ is the diffusion velocity of gas species k, $\mathbf{V}_Y$ is the diffusion velocity related to soot mass, $\mathbf{V}_N$ is the diffusion velocity related to soot number, $\dot{\omega}_k$ is the time rate of change of the kth species mass, S_Y is the time rate of change of the soot mass, S_N is the time rate of change of the soot number, τ is the fluid stress tensor, $\mathbf{g}$ is the acceleration vector due to

gravity, N is the number of gaseous species in the mixture, and $\mathbf{q}$ is the heat flux vector. The latter contains contributions from conduction, diffusion, and radiation, and is given by

$$\mathbf{q} = -\kappa \nabla T + \rho \sum_{k=1}^{N+1} h_k Y_k \mathbf{V}_k + \mathbf{q}_{\text{rad}} \tag{7}$$

where κ is the mixture thermal conductivity, h_k is the individual species enthalpy, and $\mathbf{q}_{\text{rad}}$ is the radiative heat flux, the determination of which is of particular interest in this study. In Eq. 7, and throughout this work, the $(N+1)$th species refers to soot, the enthalpy of which was approximated using the properties of graphite. The time rate of change of gaseous species includes contributions from both gas-phase chemistry and soot surface reactions.

In the computational framework developed by Charest, Groth, Gülder (2010) for the prediction of laminar flames, soot formation and destruction was modeled using the simplified soot kinetics described by Liu et al. (2002). This model is based on the reduced soot mechanisms of Leung, Lindstedt, and Jones (1991) and Fairweather, Jones, and Lindstedt (1992) which describe the evolution of soot through basic steps for nucleation, surface growth, coagulation, and oxidation. Acetylene is assumed to be the only precursor responsible for the presence of soot. Multi-species diffusion was modeled using the first-order Hirschfelder and Curtiss approximation (Hirschfelder, Curtiss, Byrd 1969) while soot was assumed to diffuse primarily by thermophoresis using a model based on the limit of free-molecular flow (Smooke et al. 1999). In addition to contributions from thermophoresis, a small Fickian diffusive flux was included in the soot particle transport equations. This procedure, which is similar to the one adopted by Kennedy, Kollmann, and Chen (1990), was required to enhance numerical stability even though the transport of soot via Brownian motion is generally negligible.

Radiation model

Detailed treatment of thermal radiation for the prediction of the divergence of the radiative heat flux, Eqs. (3) and (7), is necessary for accurate prediction of the flame structure, species concentrations, and formation of soot (Viskanta and Mengüç 1987). This require however the solution of a complex integro-differential equation describing the transport of radiant energy in physical space $\vec{x}$ and time t, in a given direction represented by the unit vector, $\vec{s}$, at a given wavenumber η. This so-called radiative transfer equation (RTE) has the form (Modest 2013)

$$\frac{1}{c}\frac{\partial I_\eta}{\partial t} + \vec{s}.\vec{\nabla} I_\eta = \kappa_\eta I_{b\eta} - (\kappa_\eta + \sigma_{s\eta}) I_\eta + \frac{\sigma_{s\eta}}{4\pi} \int_{4\pi} I_\eta(\vec{s}\,') \Phi_\eta(\vec{s}\,', \vec{s}) d\Omega', \tag{8}$$

where $\kappa_\eta = \kappa_\eta(\vec{x}, t)$ and $\sigma_{s\eta} = \sigma_{s\eta}(\vec{x}, t)$ represent the spectral absorption and scattering coefficients of the participating media, respectively, c is the speed of light in a vacuum, $I_\eta = I_\eta(\vec{x}, \vec{s}, t)$ is the spectral radiative intensity, $I_{b\eta} = I_{b\eta}(T)$ (where $T = T(\vec{x}, t)$ is the temperature field) is the spectral Planck function or blackbody intensity, Ω denotes solid angle, and $\Phi_\eta(\vec{s}\,', \vec{s})$ is the scattering phase function. The latter describes the probability that a ray traveling in direction $\vec{s}\,'$ will be scattered into direction $\vec{s}$ and is also a function of location in space and time. The subscript, η, indicates a spectrally

varying quantity. The RTE, as illustrated in Eq. (8), is a complex equation with high dimensionality (7 independent variables) for which there exists no general exact analytical solution. As such, one must therefore rely on techniques based on approximate treatments of the independent variables. The temporal and spatial dependencies can be treated using standard finite-volume techniques for hyperbolic equations. The spectral dependence of the radiative properties of real gases, which is a rather strong one, will be treated using the statistical narrow-band correlated-k (SNBCK) method (Liu, Smallwood, Gülder 2000a). For the treatment of the angular dependence of the radiative intensity distribution, different approximate models will be considered, including the discrete ordinates method, the spherical harmonics and the maximum entropy moment closures.

Discrete ordinates methods

The discrete ordinates method (Fiveland 1984) is used to transform the equation of radiative transfer into a set of PDEs with only spatial and temporal dependence. This angular discretization technique makes use of the assumption that the radiation is transported only along a finite set of discrete directions, instead of the effectively infinite number of directions allowed in Eq. (8) by a continuous representation of the solid angle. In other words, the solid angle is divided into a finite number, M, of discrete directions (or ordinates) $\vec{s}_m$, $m = 0, \ldots, M$. In this way, the RTE is transformed into a system of M coupled equations given by

$$\frac{1}{c}\frac{\partial I_{\eta,m}}{\partial t} + \vec{s}_m.\vec{\nabla} I_{\eta,m} = \kappa_\eta I_{b\eta} - (\kappa_\eta + \sigma_{s\eta}) I_{\eta,m} + \frac{\sigma_{s\eta}}{4\pi}\sum_{n=1}^{M} w_n I_{\eta,n}\Phi_\eta(\vec{s}_n, \vec{s}_m), \tag{9}$$

where $I_{\eta,m}$ is the intensity in the m^{th} direction and w_m is the quadrature weight associated with the discrete direction $\vec{s}_m$. Several quadrature rules have been developed for the DOM, including the S_N schemes of Lathrop and Carlson (1965) and the T_N schemes of Thurgood, Pollard, Becker (1995). Similar to Charest, Groth, Gülder (2010), the T_3 quadrature scheme is used in this study for the DOM simulations.

Moment closure methods for solution of the RTE

An alternative approach to the treatment of the angular dependence of the radiative intensity distribution consists of solving directly for the angular integrals of the latter. These so-called angular moments are taken with respect to angular weights $\vec{s}^{\,n} = \vec{s} \otimes \overset{n}{\ldots} \otimes \vec{s}$, $n = 0, \ldots \infty$, whose entries form a monomial basis, and have the form

$$I_\eta^{(n)}(\vec{x}, t) = \langle \vec{s}^{\,n} I_\eta(\vec{x}, \vec{s}, t) \rangle = \int_{4\pi} \vec{s}^{\,n} I_\eta(\vec{x}, \vec{s}, t)\, \mathrm{d}\Omega = \int_0^{2\pi}\int_0^{\pi} \vec{s}^{\,n} I_\eta(\vec{x}, \vec{s}, t) \sin\theta \mathrm{d}\theta \mathrm{d}\psi. \tag{10}$$

Taking angular integrals of the RTE, Eq. (8), results in a system of infinite moment equations characterizing uniquely an arbitrary distribution. Solving such an infinite system of equations is however unfeasible from a numerical point of view. Instead, one generally solves transport equations for a finite set of moments. The system of

equations for a finite set of moments can not be readily solved since the transport equation for a given moment always involves the next higher-order moment. An additional expression, relating the highest-order moment in the unclosed system of moment equations to the lower-order moments must be provided for closure. This so-called closing relation is usually obtained by approximating the underlying positive distribution in terms of the known finite set of moments. However, there exists a wide range of possible approximate forms for a positive distribution with known finite set of moments. The choice of the approximate form is generally dictated by the properties of the resulting closed system of moment equations, namely realizability of moments, hyperbolicity. A set of moments is said to be realizable if there exists a positive distribution reproducing those moments. The set of all realizable moments up to a given order n is called realizability domain and is denoted as $\mathcal{R}^n$ and is generally described by a set of inequalities on the moments called realizability conditions. In this study, approximate forms for the distribution obtained from the spherical harmonics approximation, as well as the principle of maximization of entropy, will be considered and the extension of the latter to the non-gray case is the primary focus.

Another problem that arises from the truncation to a finite set of moments is the number of moments required to reconstruct the approximated intensity distribution. In general, only the zeroth- and first-order moments, namely the radiative energy density $I_\eta^{(0)}$ and the radiative heat flux $I_\eta^{(1)}$, respectively, are of interest in engineering applications. However, the more angular moments are used to reconstruct the distribution, the wider the range of optical conditions that can be captured accurately.

Spherical harmonics P_N moment closures

In the spherical harmonics moment closure approximation (Jeans 1917), the radiative intensity distribution is expressed in terms of a series of spherical harmonics as (Modest 2013)

$$I_\eta(\vec{x},\vec{s},t) = \sum_{n=0}^{N}\sum_{m=-n}^{n} I_{\eta,n}^{m}(\vec{x},t)\,Y_n^m(\vec{s}), \tag{11}$$

where N is the order of the highest moment in the closed system, $I_{\eta,n}^{m}(\vec{x},t)$ are location-dependent coefficients, which can be directly related to the know finite set of moments, and $Y_n^m(\vec{s})$ is a spherical harmonic function of degree n and order m, and has the form

$$Y_n^m(\vec{s}) = \begin{cases} \cos(m\psi)P_n^m(\cos\theta), & \text{for } m \geq 0, \\ \sin(m\psi)P_n^m(\cos\theta), & \text{for } m < 0, \end{cases} \tag{12}$$

where $P_n^m(\cos\theta)$ is the associated Legendre polynomial.

The first-order P_1 spherical harmonics approximation provides closure to the system of transport equations for the zeroth- and first-order moments, $I_\eta^{(0)}$ and $I_\eta^{(1)}$, respectively, by approximating the distribution Eq. (11) with $N = 1$ in terms of those lower-order moments. The second-order moment $I_\eta^{(2)}$ involved in the transport equation for $I_\eta^{(1)}$ can then be directly expressed in terms of those lower-order moments, therefore providing closure.

Maximum-entropy M_N moment closures

Maximum-entropy moment closures approximate the radiative intensity distribution by a distribution that maximizes the radiative entropy

$$H_R(I_\eta) = \langle h_R \rangle = \int_{4\pi} h_R(I_\eta) d\Omega, \tag{13}$$

and has a known finite set of moments $E_\eta^{(n)}$, $n = 0, \ldots, N$, where N is the order of the highest moment in the closed system of moment equations. In Eq. (13), h_R is the radiative entropy density, which corresponds to the entropy for Bose–Einstein statistics in this case and is given by

$$h_R(I_\eta) = \frac{2k\eta^2}{c}[(n+1)\ln(n+1) - n\ln(n)], \qquad n = \frac{I_\eta}{2hc\eta^3}, \tag{14}$$

and where n is the occupation number, h and k are the Planck and Boltzmann constants, respectively. The problem of finding a distribution that maximizes the radiative entropy given by Eq. (13) and (14) and subject to the constraints that a finite set of its angular moments, $E_\eta^{(n)}$, $n = 0, \ldots, N$, are known can be reformulated as an optimization problem of the form

$$\begin{aligned} \mathcal{I}_\eta &= \arg\max_{I_\eta} H_R(I_\eta) \\ \text{s.t.} \quad \langle \vec{s}^{\,(n)} I_\eta \rangle &= E_\eta^{(n)}, \quad n = 0, \ldots, N. \end{aligned} \tag{15}$$

The Lagrangian of this optimization problem is

$$\mathcal{L}(I_\eta, \boldsymbol{\alpha}) = H_R(I_\eta) - \boldsymbol{\alpha}^T(\langle \boldsymbol{m}(\vec{s}) I_\eta \rangle - \boldsymbol{E}_\eta), \tag{16}$$

where $\boldsymbol{E}_\eta$ is a vector containing all the independent entries of $E_\eta^{(n)}$, $n = 0, \ldots, N$, $\boldsymbol{m}(\vec{s})$ is a vector containing all the independent entries of $\vec{s}^{\,(n)}$, $n = 0, \ldots, N$, and $\boldsymbol{\alpha}$ is the vector of Lagrange multipliers associated with the moment constraints. The entropy maximizing distribution, which satisfies $\partial\mathcal{L}(I_\eta, \lambda)/\partial I_\eta = 0$, then takes the form (Dubroca and Feugeas 1999)

$$\mathcal{I}_\eta(\boldsymbol{\alpha}, m) = 2hc\eta^3 \left[\exp\left(\frac{c^2 h\eta}{k} \boldsymbol{\alpha}^T m(\vec{s})\right) - 1\right]^{-1} \tag{17}$$

In Eq. (17), the radiative intensity distribution is expressed in terms of the Lagrange multipliers, $\boldsymbol{\alpha}$, which depend on the angular moments of the distribution $\boldsymbol{E}_\eta$. With the exception of the gray M_1 model (Dubroca and Feugeas 1999), there exist no analytical expression for the Lagrange multipliers in terms of the angular moments, and the former must therefore be determined numerically in terms of the latter by solving the Lagrangian dual optimization problem

$$\max_{\boldsymbol{\alpha}} \{\mathcal{L}^*(\boldsymbol{\alpha})\}, \tag{18}$$

where $\mathcal{L}^*(\boldsymbol{\alpha})$ is the Legendre transform of $\mathcal{L}(I_\eta, \boldsymbol{\alpha})$ and has the form

$$\mathcal{L}^*(\boldsymbol{\alpha}) = \frac{2k\eta^2}{c}\left\langle \log\left[\exp\left(\frac{c^2h\eta}{k}\boldsymbol{\alpha}^T m(\vec{s})\right) - 1\right]\right\rangle - \boldsymbol{\alpha}^T \boldsymbol{E}_\eta \tag{19}$$

For any given wavenumber, η, a more convenient form of the optimization problem, Eq. (18), which would allow to solve the latter independently of frequency, can be obtained by a change of variables of the form $\beta = (c^2h\eta)\boldsymbol{\alpha}/k$, such that

$$\mathcal{L}^*(\beta) = \left\langle \log\left[\exp\left(\beta^T \boldsymbol{m}(\vec{s})\right) - 1\right]\right\rangle - \beta^T \boldsymbol{E}_\eta/(C_1\eta^3/\pi), \quad \mathcal{L}^*(\boldsymbol{\alpha}) = 2ck\eta^2\mathcal{L}^*(\beta) \tag{20}$$

where $C_1 = 2\pi hc^2$ is the so-called first radiation constant. It is clear from Eq. (20) that, for constant values of the $\boldsymbol{E}_\eta/\eta^3$, maximizing $\mathcal{L}^*(\boldsymbol{\alpha})$ is equivalent to maximizing $\mathcal{L}^*(\beta)$.

First-order M_1 maximum-entropy moment closure for non-gray gas

In the system of moment equations up to first-order, the second-order moment appearing in the transport equation for the first-order moment must be expressed in terms of the lower-order moments in order to provide closure. The M_1 model assumes an entropy-maximizing distribution with known angular moments up to first order, which can then be used to provide a closure to the first-order system of moment equations. However, unlike the case for a gray gas, for a non-gray gas, an analytical expression for the closure relation cannot be obtained, and the optimization problem Eq. (20) must be solved for any given realizable set of moments in order to obtain the corresponding Lagrange multipliers and consequently the highest-order moment in the unclosed system of equations ($I_\eta^{(2)}$ in this context) by an appropriate integration of the assumed distribution. In order to avoid such expensive repeated solution of the optimization problem whenever an update of the radiation solutions is required, an approximation of the closure relation has been developed by Sarr and Groth (Sarr, Groth, Hu 2019), based on pre-computed solutions of the maximum entropy problem interpolated throughout the full realizable space, and is presented in this section. The newly developed closure appears to be realizable and hyperbolic, and therefore retains all the desirable properties of the original M_1 closure.

The M_1 system of moment equations up to first order is represented by a set of four transport equations, since the zeroth-order moment, $I_\eta^{(0)}$, is a scalar and the first-order moment, $I_\eta^{(1)}$, is a three-component vector in three dimensional space. As such, an interpolation of the closure relation in terms of the lower-order moments would require a four-dimensional interpolation. However, for first-order moment closures, the first-order angular moment is the only moment available for describing departures from equilibrium, such that, for any distribution reconstructed in terms of the moments up to first order, all the anisotropy lies in the direction of $I_\eta^{(1)}$. In such situations, the radiative intensity distribution is symmetric with respect to the direction of $I_\eta^{(1)}$. Using this property, Levermore (1984) derived an expression for the M_1 closure in multiple space dimensions, which has the form

$$N^{(2)} = \frac{1-\chi_2}{2}\vec{\vec{I}} + \frac{3\chi_2 - 1}{2}\vec{n}\otimes\vec{n}, \tag{21}$$

where $\vec{\vec{I}}$ is the identity matrix, $\vec{n} = N^{(1)}/\parallel N^{(1)} \parallel$ is a unit vector in the direction of the first-order normalized moment $N^{(1)}$, and χ_2 is the so-called Eddington factor for which there exists no exact analytical expression, except for a gray gas. For the non-gray M_1 model, which is of interest in the current study, Sarr, Groth, Hu (2019) developed an interpolative-based analytical approximation of χ_2, obtained using pre-computed solutions of Eq. (20) for sets of moments up to first order, $\boldsymbol{E}_\eta = \{I_\eta^{(0)}, I_\eta^{(1)}\}$, spanning the full realizable space $\mathcal{R}^1$, the latter being defined as follows

$$\mathcal{R}^1 = \{(I_\eta^{(0)}, I_\eta^{(1)}) \quad \text{s.t.} \quad I_\eta^{(0)} > 0 \quad \text{and} \quad ||N^{(1)}|| \leq 1\} \tag{22}$$

where $N^{(i)} = I_\eta^{(i)}/I_\eta^{(0)}$ is the i^{th}-order normalized moment. On the boundaries of $\mathcal{R}^1$, denoted here by $\partial\mathcal{R}^1$ and defined as

$$\partial\mathcal{R}^1 = \{(I_\eta^{(0)}, I_\eta^{(1)}) \quad \text{s.t.} \quad I_\eta^{(0)} \to 0 \quad \text{or} \quad I_\eta^{(0)} \to \infty \quad \text{or} \quad ||N^{(1)}|| = 1\}, \tag{23}$$

the optimization problem given by Eq. (20) cannot be solved since the corresponding entropy maximizing distribution Eq. (17) becomes singular with respect to one of its angular moments. More specifically, on $\partial\mathcal{R}^1$, the radiative intensity distribution is either uniquely determined by a Dirac-delta distribution (for $\parallel N^{(1)} \parallel = 1$), or tends toward a particular form in the limit where $I_\eta^{(0)} \to 0$ or $I_\eta^{(0)} \to \infty$. In fact, for $I_\eta^{(0)} \to 0$ (corresponding to the so-called hyperbolic limit), the exponential term in Eq. (17) becomes very large, in which case the subtracted term can be neglected. On the other hand, for $I_\eta^{(0)} \to \infty$ (referred to as the logarithmic limit), the exponential term in Eq. (17) becomes small, in which case the exponential can be expanded in a first-order Taylor series (Cernohorsky and Bludman 1994). Based on the above, pre-computed maximum-entropy solutions throughout the full realizable space $\mathcal{R}^1 = int\mathcal{R}^1 \cup \partial\mathcal{R}^1$ can be obtained by solving the optimization problem for entropy maximization corresponding to the appropriate form of the distribution in $int\mathcal{R}^1$ and $\partial\mathcal{R}^1$. Pre-computed values of the Eddington factor, for 100 values of r equally distributed between [0, 1] and 100 values of $\parallel N^{(1)} \parallel$ equally distributed between [0, 1], where $r(I_\eta^{(0)}) = I_\eta^{(0)}/(I_\eta^{(0)} + C_1\eta^3)$ is a normalization parameter for the radiative energy density, $I_\eta^{(0)}$, such that $r \in [0, 1]$ for $I_\eta^{(0)} \in [0, \infty]$, are illustrated in Figures 1 and 2.

The approximate form of χ was chosen as a convex interpolation between the isotropic limit ($\parallel N^{(1)} \parallel = 0$) and the free streaming limit ($\parallel N^{(1)} \parallel = 1$) having the form

$$\chi_2(I_\eta^{(0)}, \parallel N^{(1)} \parallel) = \frac{1}{3} + \frac{2}{3} f(r(I_\eta^{(0)}), \parallel N^{(1)} \parallel), \tag{24}$$

where $f(r(I_\eta^{(0)}), \parallel N^{(1)} \parallel)$ represents the convex interpolant. The latter is defined such that $\chi_2(I_\eta^{(0)}, \parallel N^{(1)} \parallel)$ is exact in the isotropic and free-streaming limits, i.e., $\chi_2(I_\eta^{(0)}, 0) = 1/3$ and $\chi_2(I_\eta^{(0)}, 1) = 1$, and reproduces pre-computed values obtained by solving Eq. (20) for

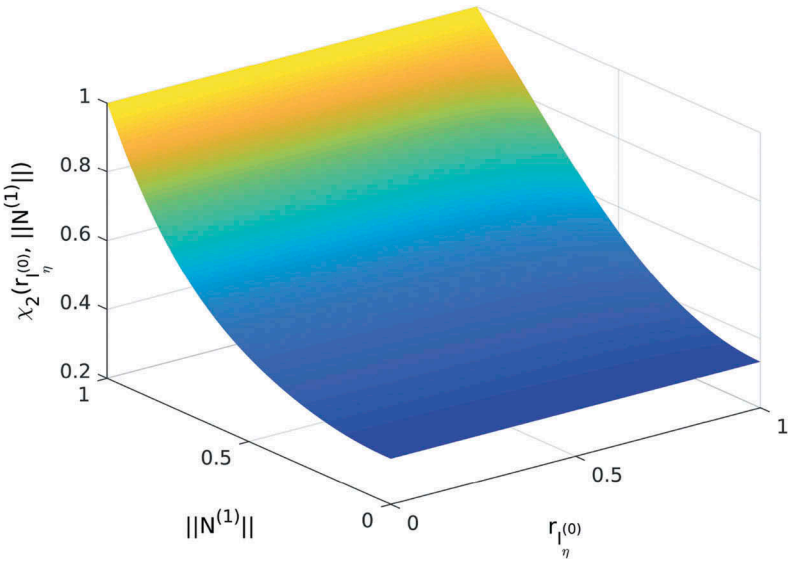

Figure 1. Eddington factor corresponding to non-gray first-order maximum entropy (M_1) moment closure for all realizable sets of moments $\{I_\eta^{(0)}, I_\eta^{(1)}\}$.

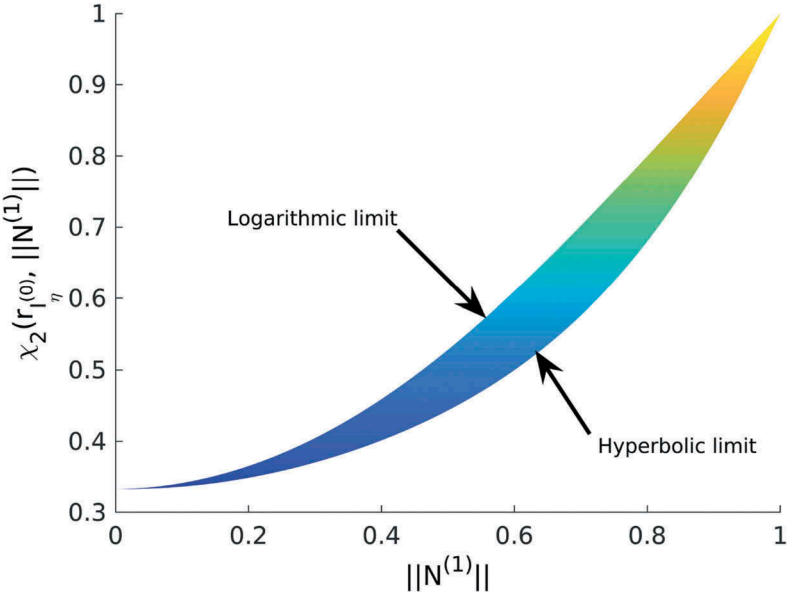

Figure 2. Eddington factor corresponding to non-gray first-order maximum entropy (M_1) moment closure for all realizable sets of moments $\{I_\eta^{(0)}, I_\eta^{(1)}\}$.

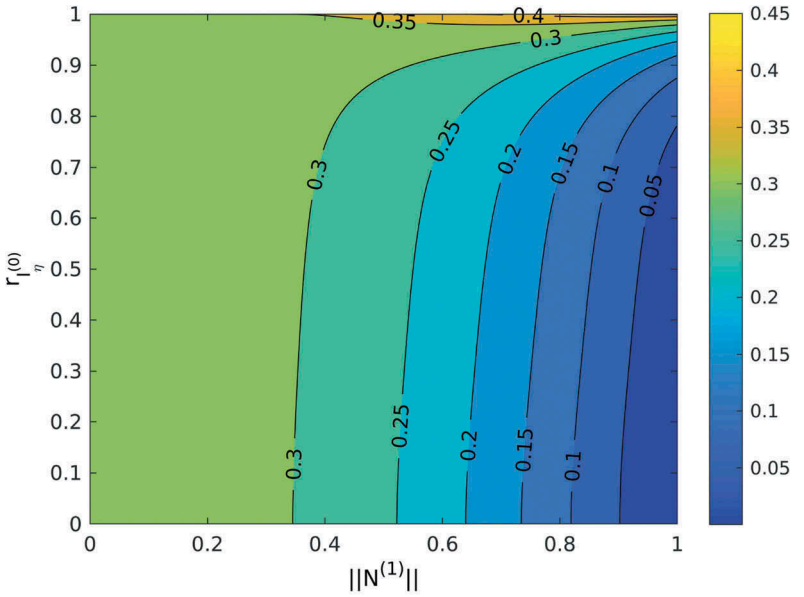

Figure 3. Realizability contours for the non-gray M_1 closure for sets of moments $\{I_\eta^{(0)}, I_\eta^{(1)}\}$ spanning the whole realizability domain.

sets of moments spanning $\mathcal{R}^1$. Moreover, in order to guarantee realizability of the approximated $\chi_2(I_\eta^{(0)}, \| N^{(1)} \|)$, we also choose $f(r(I_\eta^{(0)}), \| N^{(1)} \|)$ such that the derivatives of the Eddington factor in the free-streaming limit are exactly reproduced. In fact, as can be seen in Figure 4, in the free-streaming limit, the upper and lower boundaries of the realizability domain for χ_2 approach one another, and, therefore, the margin for the error of the approximation of χ_2 becomes smaller. Computing the derivatives of χ with respect to $\| N^{(1)} \|$ in the free-streaming limit yields the following results

$$\frac{\partial \chi}{\partial \| N^{(1)} \|} = \begin{cases} 1 & \text{for} \quad I_\eta^{(0)} \to 0 \\ 2 & \text{for} \quad I_\eta^{(0)} \to \infty \end{cases} \tag{25}$$

Based on the above requirements, the following expression for $f(r, \| N^{(1)} \|)$ is chosen

$$f(r, \| N^{(1)} \|) = \| N^{(1)} \|^{\theta(r, \| N^{(1)} \|)}, \tag{26}$$

where $\theta(r, \| N^{(1)} \|)$ is a polynomial expression of the form

$$\theta(r, \| N^{(1)} \|) = \sum_{i=0}^{n_i} \sum_{j=0}^{n_j} r^i \| N^{(1)} \|^{2j} D_{ij} \tag{27}$$

and where D_{ij}, $i = 0, \ldots, n_i$, $j = 0, \ldots, n_j$, are some coefficients that are determined such that the proposed approximation of the Eddington factor, Eq. (24), exactly reproduces the derivatives in the free-streaming limit, given in Eq. (25), and approximates pre-computed

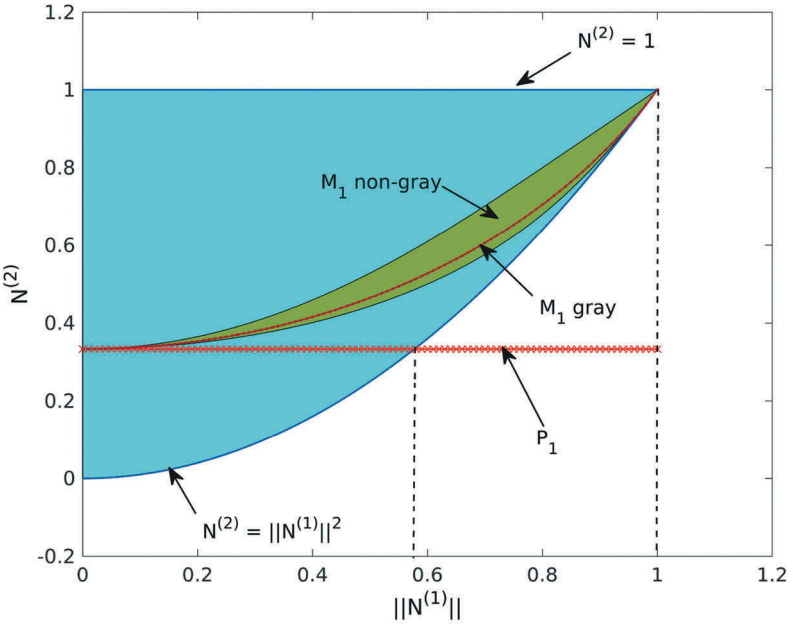

Figure 4. Eddington factor corresponding to non-gray first-order maximum entropy (M_1) moment closure for all realizable sets of moments $\{I_\eta^{(0)}, I_\eta^{(1)}\}$.

values in the interior of the domain via curve fitting. The maximum error between the proposed interpolative-based M_1 closure of (Sarr, Groth, Hu 2019), Eq. (24), and the pre-computed values of χ is 7.38×10^{-3} for $n_i = 5$ and $n_j = 4$.

The behavior of the approximation, which consists of an approximation in the hyperbolic and logarithmic limits, followed by an approximation through the whole range of possible values for r (r from 0 to 1), is illustrated in Table 1.

The realizability of the newly developed interpolative closure for sets of moments $\{I_\eta^{(0)}, I_\eta^{(1)}\}$ spanning the whole realizability domain $\mathcal{R}^1$, which constraints the Eddington factor, χ, as follows

$$\| N^{(1)}\|^2 < \chi_2(I_\eta^{(0)}, \| N^{(1)} \|) < 1, \tag{28}$$

is assessed by computing the parameter

$$f = \frac{\chi_2(I_\eta^{(0)}, \| N^{(1)} \|) - \| N^{(1)}\|^2}{1 - \| N^{(1)}\|^2}, \tag{29}$$

for sets of moments $\{I_\eta^{(0)}, I_\eta^{(1)}\}$ spanning $\mathcal{R}^1$. As illustrated in Figure 3, it would appear that the newly developed interpolative approximation of the non-gray M_1 closure, Eq. (24), is realizable, i.e., satisfies Eq. (28), since $0 \leq f \leq 1$ everywhere in $\mathcal{R}^1$.

Table 1. Non-gray M_1 closure approximation.

Boundary	Fit Error
$r \to 0$	5.43×10^{-4}
$r \to 1$	4.49×10^{-4}
$r \in [0,\ 1]$	7.38×10^{-3}

Implementation using narrow-band correlated-*k* absorption model

The RTE, as defined in Eq. (8), represents the transport of radiation for a single wavenumber. In reactive flows, however, the radiative properties of participating gases, in particular the absorption coefficient, varies strongly throughout the spectrum. The statistical narrow-band correlated-*k* (SNBCK) model is employed in this study in order to treat such strong spectral dependence. In the SNBCK model, the spectral domain is divided into bands of frequencies of size $\Delta\eta$. The size of the bands is chosen to be sufficiently small such that the Planck function, $I_{b\eta}$, can be assumed to be constant within each band. A cumulative distribution function for the absorption coefficient, $g(k)$, which can be interpreted as a dimensionless wavenumber coordinate varying between 0 and 1, is then introduced. This cumulative distribution function allows for the reordering of the strongly spectrally varying absorption coefficient into a monotonic function, such that the number of evaluations of the RTE, Eq. (8), that is required for accurate integration over each narrow-band is substantially reduced in comparison to classical line-by-line calculations. Assuming a non-scattering medium, the RTE, Eq. (8), integrated over each narrow band, yields

$$\int_0^1 \frac{1}{c}\frac{\partial I_g}{\partial t}dg + \int_0^1 \vec{s}.\vec{\nabla} I_g dg = \int_0^1 k(g)(I_{b\eta_c} - I_g)dg, \tag{30}$$

where

$$I_g = \frac{\int_{\Delta\eta} I_\eta \delta(k-\kappa_\eta)d\eta}{\int_{\Delta\eta} \delta(k-\kappa_\eta)d\eta} \tag{31}$$

and where $I_{b\eta_c}$ is the Planck function evaluated at the wavenumber corresponding to the band center, denoted herein by η_c.

In the context of the statistical narrow-band correlated-*k* model considered herein, the cumulative distribution function, $g(k)$, is obtained by taking the inverse Laplace transformation of the statistical narrow-band transmissivity (Lacis and Oinas 1991), the construction of which is based on the narrow-band data of Soufiani and Taine (Soufiani and Taine 1997) for H_2O, CO_2, and CO. In order to achieve computational savings, the three radiating gases are approximated by a single gas with effective narrow-band parameters based on the optically thin limit (Liu, Smallwood, Gülder 2000a). In addition, the band lumping procedure described by Liu *et al.* (Liu, Smallwood, Gülder 2000b) was adopted, whereby several bands are combined to form wide bands. A total of nine non-uniformly

spaced wide bands were then employed based on the recommendation of Goutiere, Charette, Kiss (2002).

The integration over the narrow-bands is performed by means of Gauss-Legendre quadrature, such that the spectrally integrated intensity for each band is computed as

$$\overline{I_{\Delta\eta}} = \sum_{i=1}^{N_g} w_i I(g_i), \tag{32}$$

where N_g is the umber of Gauss quadrature points and w_i are the weights. Liu, Smallwood, & Gülder, (2000a) found that four Gauss quadrature points provide a good balance between accuracy and computational costs. The divergence of the radiative heat flux, also referred to as the radiative source term, is then evaluated as

$$\nabla . q_{rad} \approx \sum_{j=1}^{N_b} \sum_{i=1}^{N_g} w_i \kappa(g_i)(4\pi I_{b\eta_{cj}} - \langle I(g_i)\rangle)\Delta\eta_j \tag{33}$$

where N_b is the number of narrow bands, $\Delta\eta_j$ is the width of the jth narrow-band, and $\langle I(g_i)\rangle$ represents the angular integral (see Eq. (10)) of the intensity distribution obtained by solving the RTE at quadrature point g_i. An estimate of the underlying intensity distribution or its angular moments in this context can be easily obtained using either the DOM or the P_N moment closures. However, for the newly developed non-gray M_1 closure, for which we proposed an interpolative-based analytical approximation of the Eddington factor, Eq. (24), coupling with the SNBCK represents additional challenges due to the explicit wavenumber dependence of the resulting Eddington factor. However, a close inspection of the entropy maximizing distribution, Eq. (17), shows that it has the same form as the Planck function, the only difference being to the Lagrange multipliers in the exponential terms which allow departures from equilibrium (or the Planck function distribution or isotropic distribution). As such, similar to how the Planck function is assumed to be essentially constant within a narrow-band, it would also seem reasonable to assume that the entropy maximizing distribution is also constant and can be evaluated at the wavenumber corresponding to the band center.

For the sooting flames of interest, the absorption due to soot particulate matter must also be accounted for. The spectral absorption coefficient of soot, which is determined in the Rayleigh limit for small spherical particles (Modest 2013), is used here and given by

$$\kappa_{\eta,\text{soot}} = C f_v \eta, \tag{34}$$

where f_v is the soot volume fraction and C is an empirical constant, which is taken to be 5.5, similar to the value used by Liu *et al.* (Liu et al. 2002).

Finite-volume method

Similar to the more common P_N spherical harmonics moment closures, the newly developed non-gray M_1 closure is hyperbolic, since its eigenvalues are real everywhere in $\mathcal{R}^1$. This important property of the M_1 closure makes the corresponding closed system of

moment equations very well suited for solution by the now standard family of upwind finite-volume (FVM) techniques originally developed by Godunov (Godunov 1959) for hyperbolic systems of conservation laws. More specifically, similar to the conservation equations in the computational framework for laminar reactive flows developed by Charest, Groth, Gülder (2010), the conservation equations for the M_1 closure are solved using the parallel, implicit, upwind Godunov-type finite-volume scheme described by Groth and coworkers (Gao, Northrup, Groth 2011; Sachdev, Groth, Gottlieb 2005). The scheme solves the conservation form of the moment equations on body-fitted, multi-block, quadrilateral meshes by discretizing the physical domain into finite-sized quadrilateral-shaped computational cells. The integral forms of conservation laws are then applied to each individual cell, thereby resulting in a coupled system of nonlinear ordinary differential equations (ODEs) for cell-averaged solution quantities. The numerical fluxes at the cell interfaces are evaluated using the Harten, Lax, Van Leer – Einfeldt (HLLE) (Einfeldt 1988; Harten 1983) approximate Riemann solver. Finally, steady-state solutions were obtained using an implicit Newton–Krylov Schwarz (NKS) iterative algorithm with General Minimal Residual (GMRES) method for the associated linear system, the implementation of which has been developed previously by Groth and Northrup (2005) as well as Charest, Groth, Gülder (2010, 2012) for computations on large multi-processor parallel clusters.

Numerical results for laminar co-flow diffusion flames

In an effort to further assess the predictive capabilities of the proposed interpolative-based analytical approximation of the non-gray M_1 maximum-entropy moment closure, comparisons of its solutions in numerical simulations of laminar diffusion flames to those obtained using the P_1 moment closure and the DOM were performed. Two different types of flames were considered: the methane-air co-flow diffusion flames and the ethanol-methane flames for pressures up to 4 atm of Griffin, Christensen, Gülder (2018). The computational framework used here for predicting soot formation in laminar reactive flows was previously developed by Charest, Groth, Gülder (2010). The latter has been previously used to predict soot formation in elevated pressure laminar diffusion flames for a variety of fuels ranging from ethylene (Charest et al. 2011), methane (Charest, Groth, Gülder 2011), and biogas (Charest, Gülder, Groth 2014). As described above, the statistical narrow-band correlated-*k* (SNBCK) model (Liu, Smallwood, Gülder 2000a) was used for the treatment of the spectral dependence of absorbing gases. Additionally, the reduced Princeton mechanism (Akih-Kumgeh 2013) was used to model the chemical kinetics for the fuels of interest as it provides a good balance between accuracy and computational expenses. The configuration of the burner, which was used for both types of flames, is first described, followed by the details of the calculations, and finally the numerical results obtained for the cases of interest are presented and discussed.

High-pressure co-flow burner configuration

The laboratory-scale, high-pressure axisymmetric burner for laminar co-flow flames (Joo and Gülder 2009) considered in this study consists of a central fuel tube with 3 mm inner

diameter and a concentric tube of 25.4 mm inner diameter that supplies the co-flow air, as illustrated in Figure 5. In order to minimize the formation of wakes behind the tube walls and improve overall flame stability, the outer surface of the fuel nozzle was tapered. Moreover, a sintered metal foam was inserted in both the fuel and air nozzles so as to straighten the flow and provide a more uniform velocity profile at the nozzle exit. Experimental measurements of temperature and soot for mixtures of ethanol and methane at different pressures were previously performed by (Griffin, Christensen, Gülder 2018) for pressures of 1, 2, 4, and 6 atm. The temperature of the fuel and air supplied to the burner was assumed to be equal to 473K and the air mass flow rate was kept constant at 340 mg/s for all cases. For all the flames, the mass flow rates of methane and ethanol were chosen such that a constant carbon mass flow rate of 0.914 mg/s was maintained.

Computational domain and boundary conditions

The two-dimensional computational domain used for the numerical simulations of co-flow diffusion flames in the burner previously described is shown schematically in Figure 6 along with the applied boundary conditions. The domain extends radially outwards 20 mm and downstream 25 mm. It also extends 9 mm upstream into the fuel and air tubes to account for the effects of fuel preheating (Guo et al. 2002) and better represent the inflow velocity distribution. A simplified representation of the fuel tube geometry was used for computational purposes, in which the chamfered edge of the fuel tube was approximated by a tube with 0.4 mm uniformly thick walls. The three surfaces that lie along the tube wall were modeled as adiabatic walls at 300 K with zero-slip conditions on velocity. Reflection boundary conditions are applied along the centerline. The far-field boundary was treated using a free-slip condition, which neglects any shear

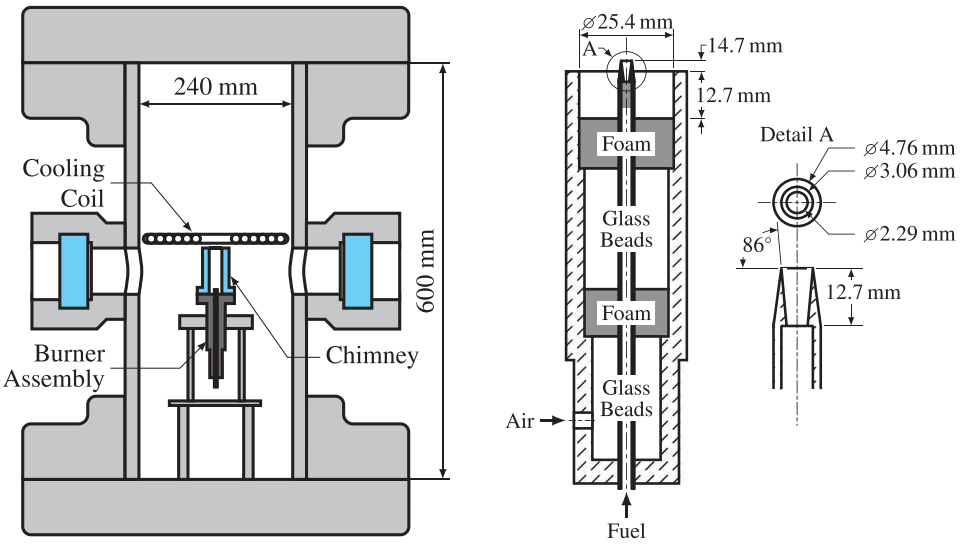

Figure 5. Schematic of the pressure vessel combustion apparatus used in the experiments conducted by Joo and Gülder (2009).

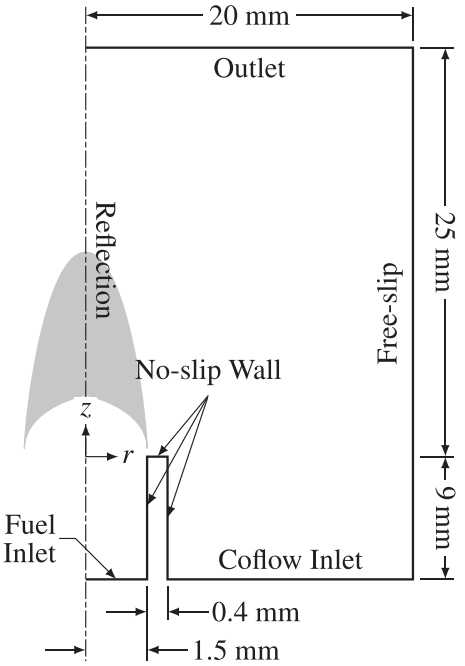

Figure 6. Computational domain and boundary conditions.

imparted by the chimney walls to the co-flow air. At the outlet, temperature, velocity, species mass fractions, and soot number density are extrapolated while pressure is held fixed. The gas/soot mixture is specified at the inlet along with its velocity and temperature while pressure is extrapolated. For the radiation solvers, all boundaries except for the axis of symmetry (for which axisymmetric boundary conditions are prescribed) are assumed to be black. More specifically, for the moment closure techniques, the partial moments boundary conditions described by Sarr, Groth, Hu (2019) were used for black surfaces, whereas the axisymmetric boundary conditions based on incoming partial moments were used for the axis of symmetry.

The computational domain depicted in Figure 6 was subdivided into 192 cells and 16 blocks in the radial- and 320 cells and 32 blocks in the axial-direction to form a structured, non-uniformly-spaced mesh of 60000 cells. These cells were clustered toward the burner exit plane to capture interactions near the fuel tube walls and toward the centerline to capture the core flow of the flame. A fixed mesh spacing of approximately 35 μm was specified in the radial-direction between $r = 0$ and $r = 4.8$ mm. The vertical spacing approaches 5.6 μm near the fuel tube exit plane. The resulting mesh, which was employed for all calculations in the present study, is illustrated in Figure 7. This level of mesh resolution, which was used previously by Charest, Groth, Gülder (2010), was shown to be more than sufficient in order to capture the essential features of the laminar co-flow diffusion flames associated with the high-pressure burner.

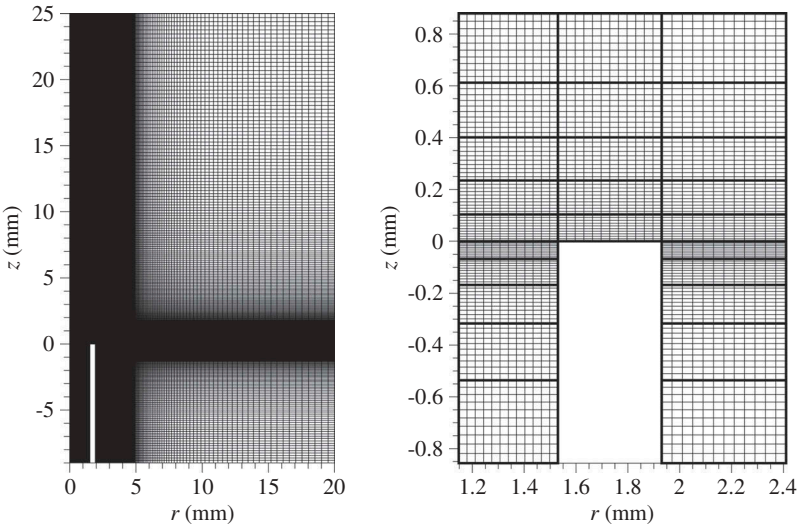

(a) Entire domain (b) Closeup of fuel tube region

Figure 7. Computational grid used for all flame calculations. Block boundaries are shown in 2 designated by bold lines.

Methane-air co-flow flames

The first set of comparisons for the M_1 moment closure involves pure methane-air co-flow flames, for which the methane mass flow rate is held at 1.221 mg/s in order to maintain the carbon flow rate at 0.914 mg/s. Laminar diffusion flames of pure methane were then simulated for pressures up to 4 atm, and the predicted two-dimensional distributions of the temperature and soot volume fraction obtained in the absence of radiative transfer (i.e., the radiative heat transfer was set to zero in the simulation) and using the non-gray M_1 maximum-entropy moment closure are both depicted for the four flames for pressures of 1, 2, 3, and 4 atm in Figure 8, 11, 14, and 17. The predicted two-dimensional distributions of the temperature and soot volume fraction obtained using the P_1 and DOM approaches were found to be very similar and are not shown. Additionally, the predicted radial profiles of temperature and soot volume fraction at different axial locations above the burner obtained using the M_1 and P_1 closures, as well as the DOM, are presented in Figure 9, 10, 12, 13, 15, 16, 18, and 19 for pressures of 1, 2, 3, and 4 atm. In addition to the approximate radiation models presented in this study, numerical results for the radial profile comparisons include results obtained for a simulation in which radiation is neglected in order to assess the relative importance of radiation for these flames. The experimental measurements of soot volume fraction and temperature obtained by (Griffin, Christensen, Gülder 2018) for the 1, 2, and 4 atm flames are also included in the radial profile comparisons.

From the simulation results of Figure 8, 11, 14, and 17, it is evident that the simulated flames reproduce the established expected structure of the laminar co-flow flames with increasing pressure (i.e., the flame height remains constant for constant carbon mass flow and the flame narrows and exhibits stronger inward radial flow as the pressure is

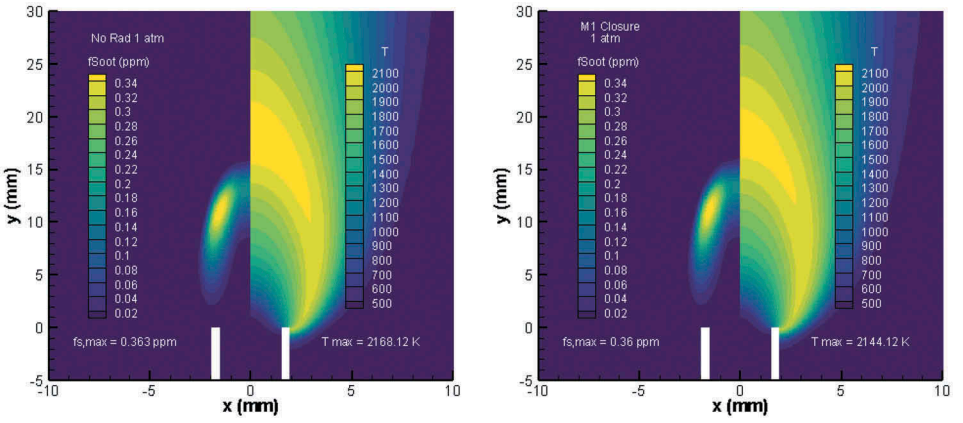

(a) Solution with no radiation (b) M_1 solution

Figure 8. Comparison of contours of temperature and soot volume fraction predicted by a) the case where radiation is neglected b) the M_1 closure for methane at 1 atm.

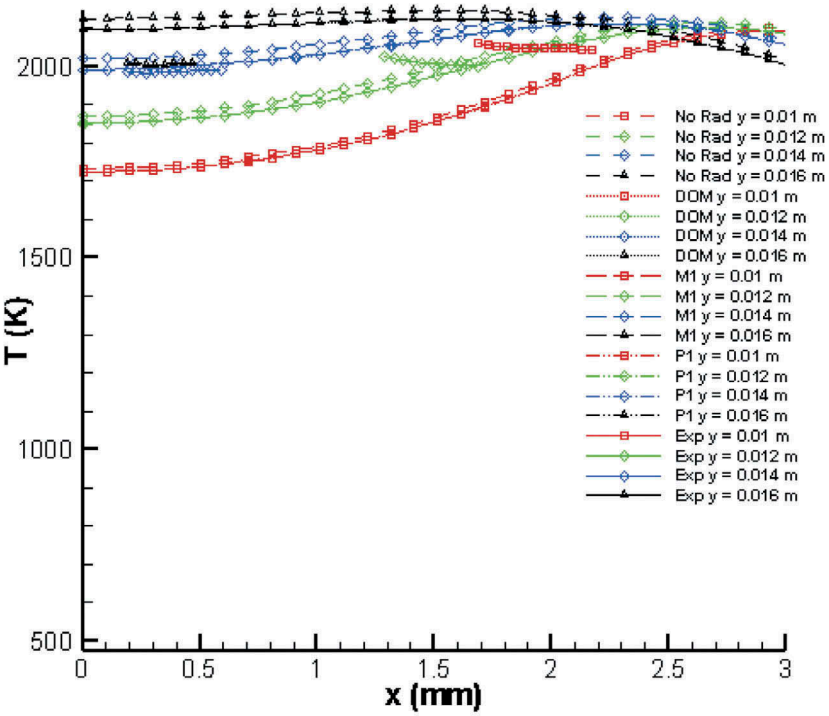

Figure 9. Radial profiles for temperature at different axial locations at 1 atm.

increased). The expected increase in the maximum soot volume fraction is also reproduced with increasing pressure. Furthermore, in the absence of radiation, the predicted temperature field is systematically overestimated, which becomes more important as pressure increases. Moreover, the predicted soot volume fraction in the case where

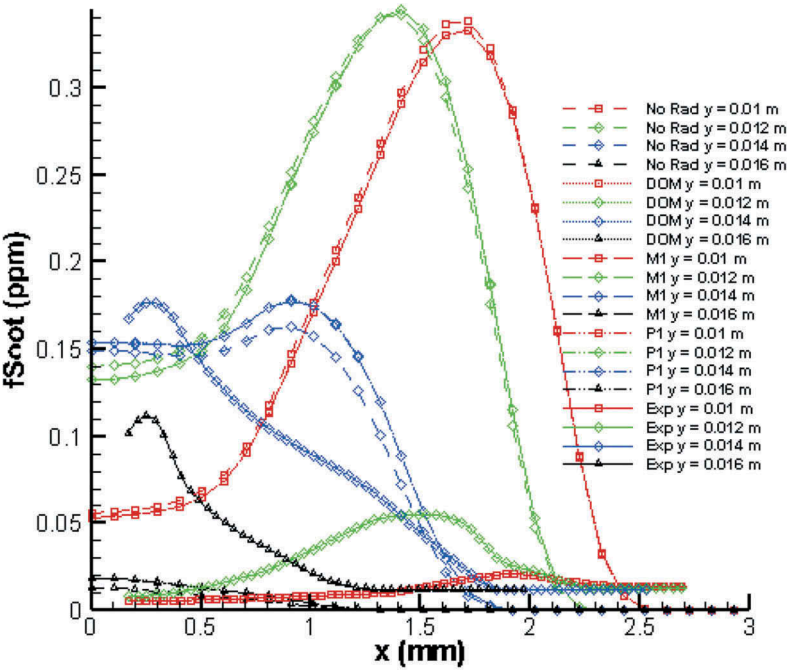

Figure 10. Radial profiles for soot volume fraction at different axial locations at 1 atm.

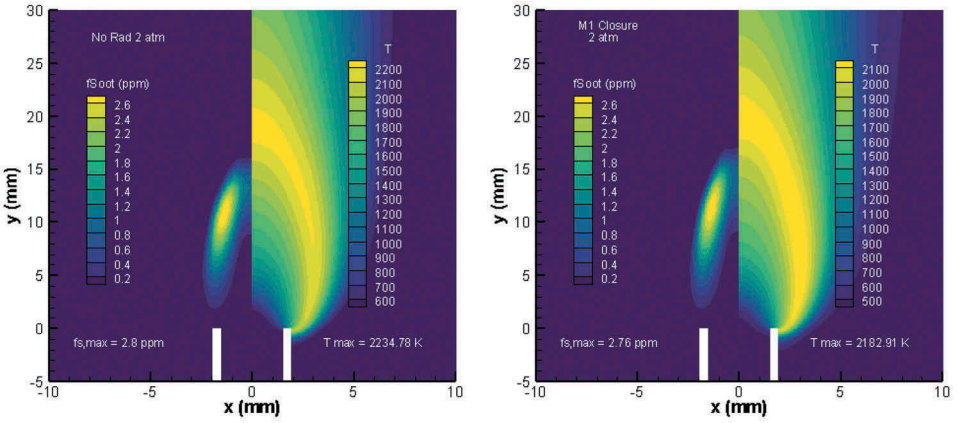

(a) Solution with no radiation (b) M_1 solution

Figure 11. Comparison of contours of temperature and soot volume fraction predicted by a) the case where radiation is neglected b) the M_1 closure for methane at 2 atm.

radiation was neglected is also overestimated upstream and correspondingly underestimated downstream of the burner. It is also evident from the results of Figure 9, 10, 12, 13, 15, 16, 18, and 19 that the predictions of the temperature and soot volume fraction radial profiles for the interpolative-based M_1 closure of Sarr, Groth, Hu (2019) is in very good

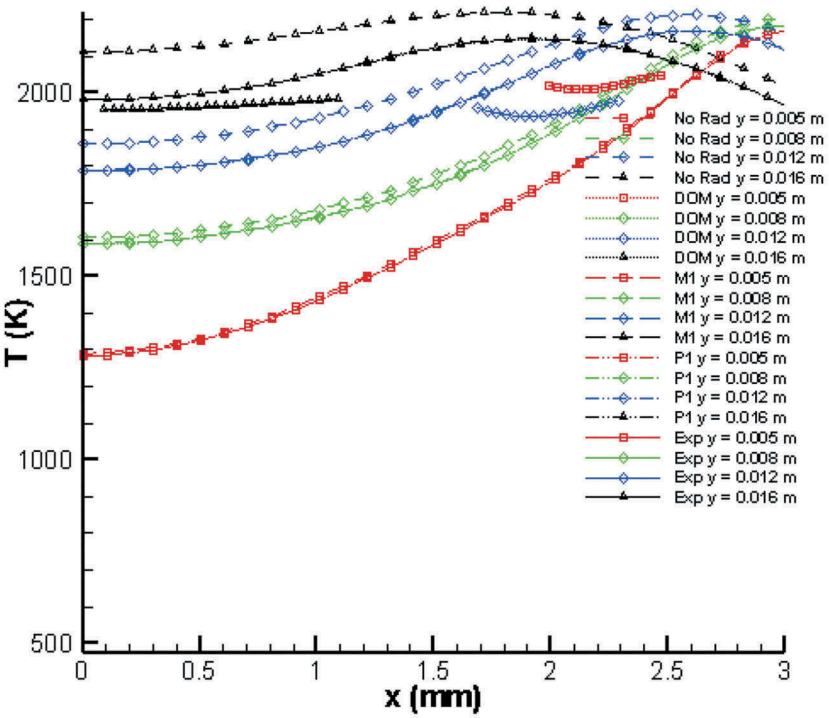

Figure 12. Radial profiles for temperature at different axial locations at 2 atm.

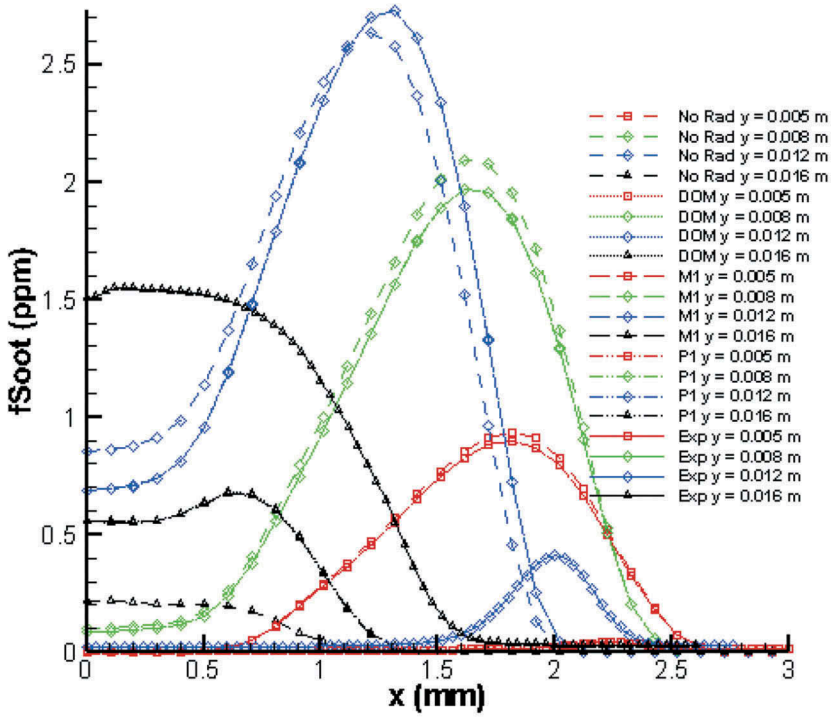

Figure 13. Radial profiles for soot volume fraction at different axial locations at 2 atm.

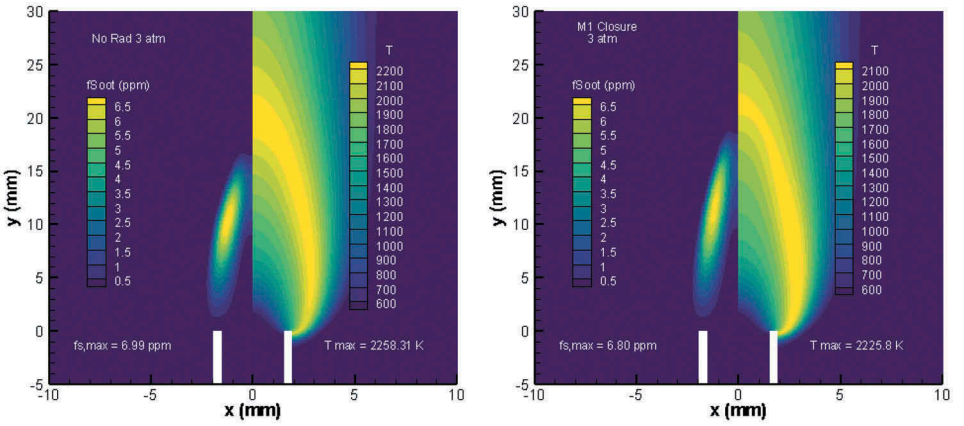

(a) Solution with no radiation (b) M_1 solution

Figure 14. Comparison of contours of temperature and soot volume fraction predicted by a) the case where radiation is neglected b) the M_1 closure for methane at 3 atm.

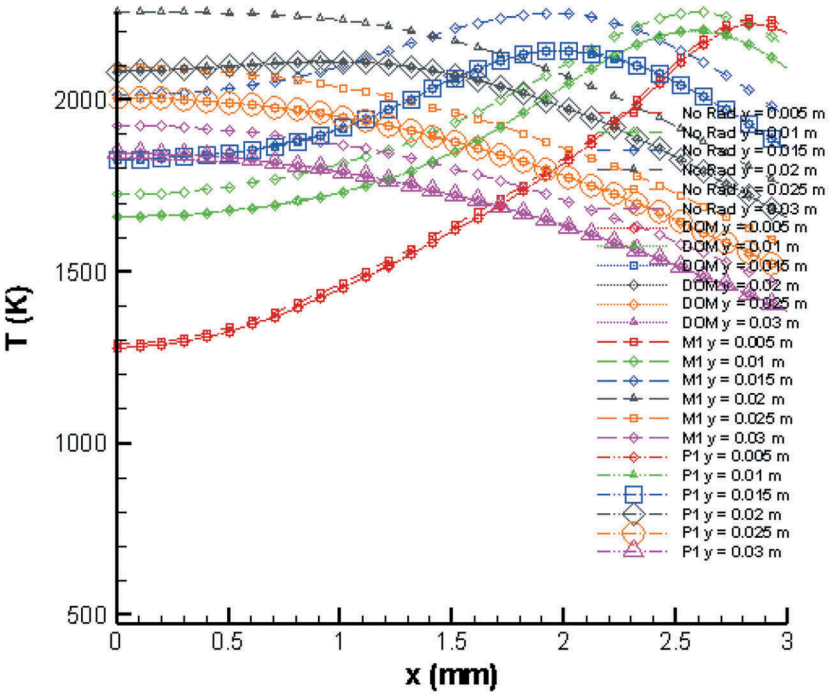

Figure 15. Radial profiles for temperature at different axial locations at 3 atm.

agreement with the predictions of both the P_1 closure and the DOM T_3 method at all axial locations and all pressures considered.

The comparisons of numerical results with the experimental data for the methane-air flames show that, at low pressures closer to the burner rim, the radial profiles of soot

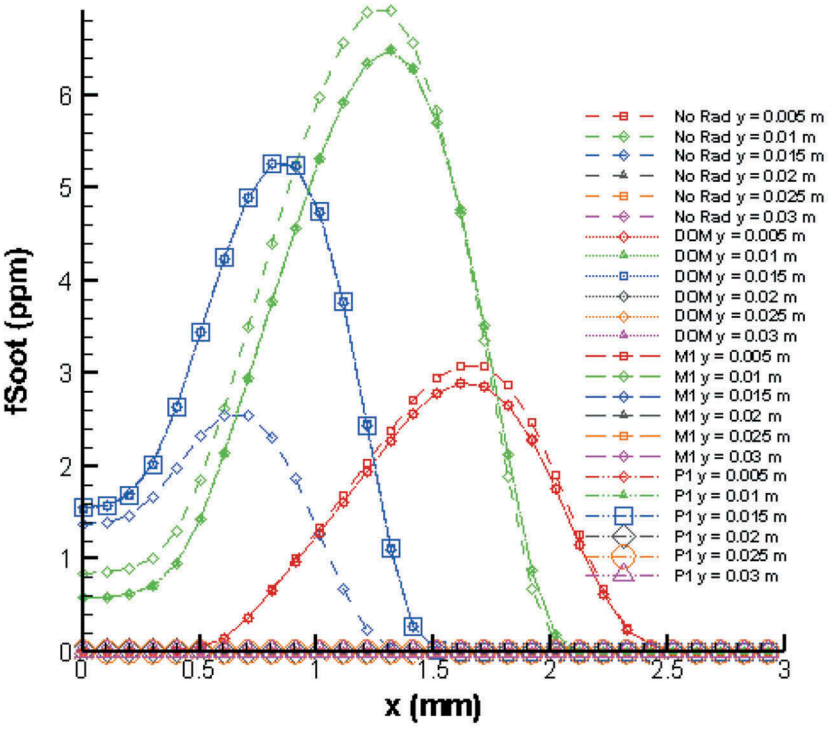

Figure 16. Radial profiles for soot volume fraction at different axial locations at 3 atm.

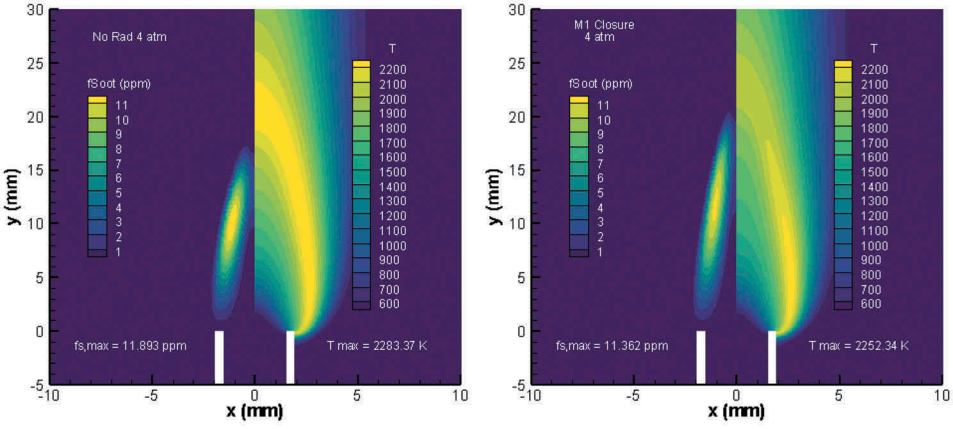

(a) Solution with no radiation (b) M_1 solution

Figure 17. Comparison of contours of temperature and soot volume fraction predicted by (a) the case where radiation is neglected (b) the M_1 closure for methane at 4 atm.

volume fraction as well as the radial locations where the peak soot concentrations occur are rather well predicted by all three radiations models (M_1 and P_1 closures as well as DOM); however, the peak values are significantly over-predicted. Further downstream of the burner rim, the numerical results obtained using all three models predict similar peak

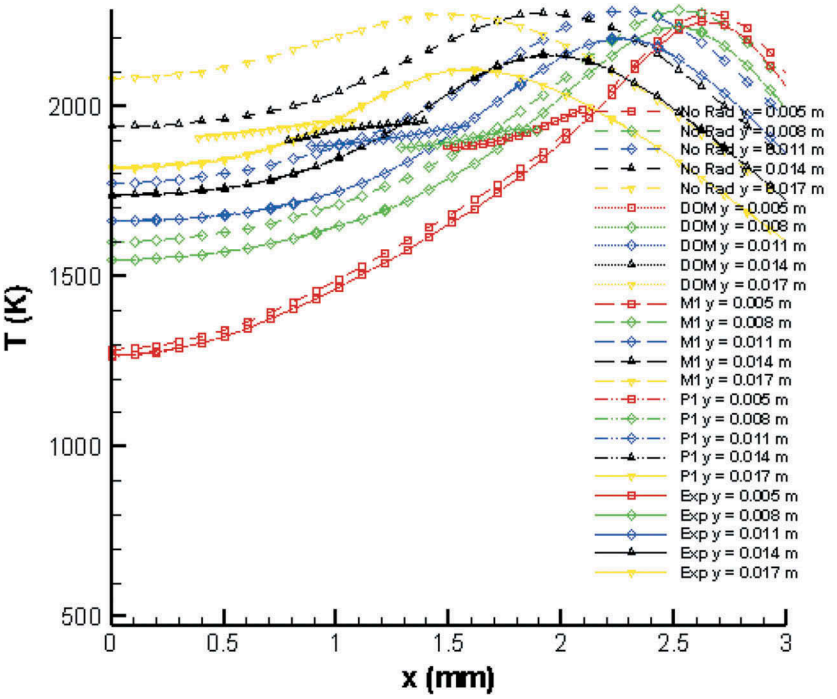

Figure 18. Radial profiles for temperature at different axial locations at 4 atm.

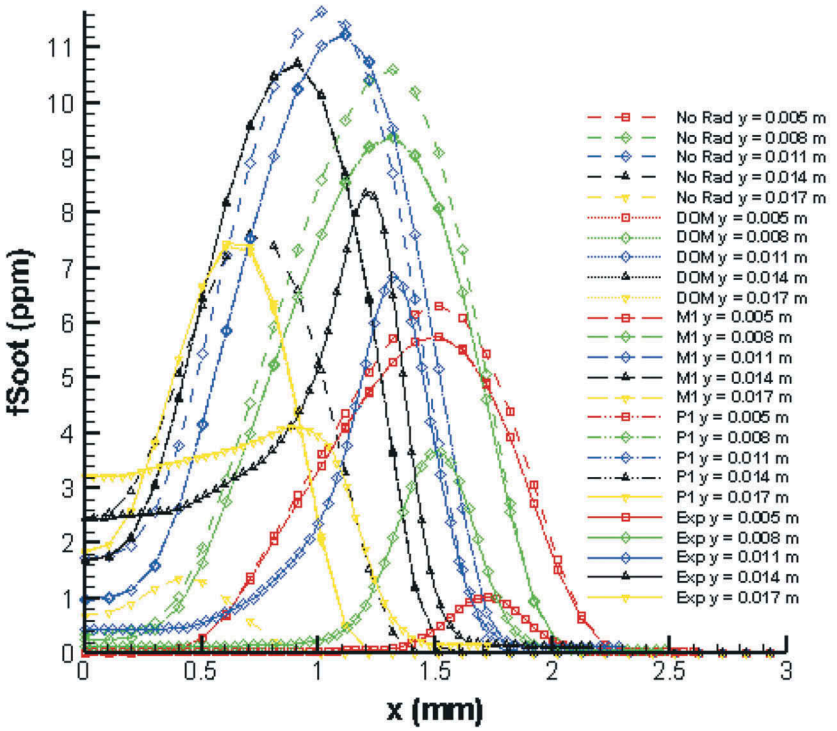

Figure 19. Radial profiles for soot volume fraction at different axial locations at 4 atm.

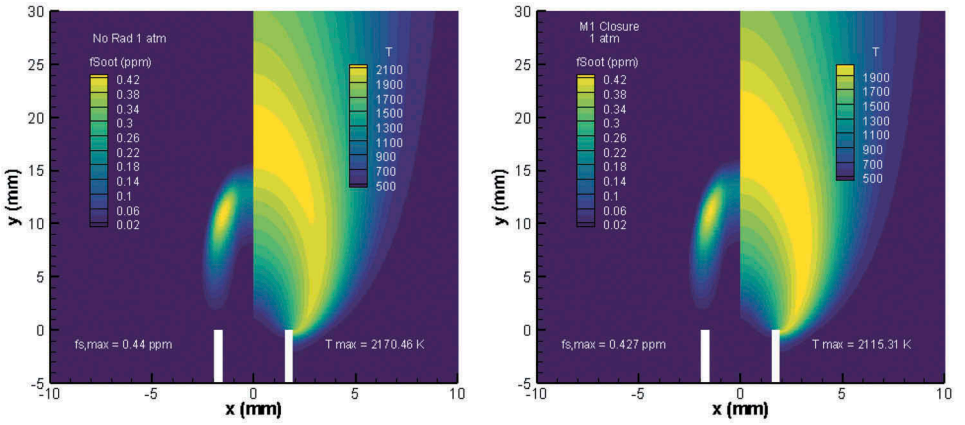

(a) Solution with no radiation (b) M_1 solution

Figure 20. Comparison of contours of temperature and soot volume fraction predicted by (a) the case where radiation is neglected (b) the M_1 closure for a mixture of methane and ethanol at 1 atm.

values for the soot volume fraction to that observed in the experiments, even though the radial location of the peak is predicted at a larger radius. As pressure increases, many of the experimentally observed trends are still predicted by the models; however, all of the models still over-predict the values of peak soot volume fraction closer to the rim, while, further downstream, an under-prediction of the peak values is observed. Moreover, the radial locations at which the peaks occur are shifted radially inward.

Methane-ethanol-air co-flow flames with 10% carbon flow contribution from ethanol

Comparisons are now considered for high-pressure laminar co-flow flames for a mixture of ethanol, methane, and air. The fuel mixture is such that 10% of the total carbon flow is contributed by ethanol. As such, the methane and ethanol mass flow rates were held at 1.099 and 0.175 mg/s, respectively, in order to match the target carbon mass flow rate of 0.914 mg/s. The predicted contours of the flame temperature and soot volume fraction for the ethanol-methane co-flow flames at pressures from 1 to 4 atm are given in Figure 20, 23, 26, and 29. As for the pure methane fuel flames, results are given for the M_1 moment closure and for the case with no radiative heat transfer. Furthermore, Figure 21, 22, 24, 25, 27, 28, 30, and 31 provide comparisons of the predicted radial profiles of temperature and soot volume fraction at different axial location above the burner, both in the presence and the absence of radiation. Results for all three radiation models are shown in the radial profiles. Additionally, the experimental measurements of soot volume fraction and temperature obtained previously by Griffin *et al.* (Griffin, Christensen, Gülder 2018) for the ethanol-methane flames are also provided for reference comparisons.

Similar to the findings for the pure methane-air flames, the overall co-flow flame structure as a function of pressure is well reproduced by the simulations obtained using

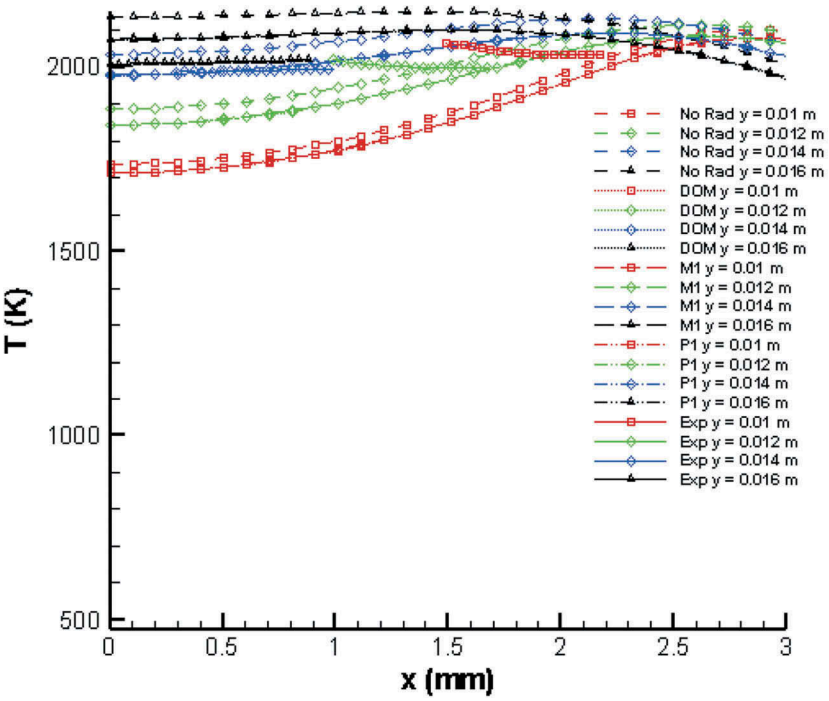

Figure 21. Radial profiles for temperature at different axial locations at 1 atm.

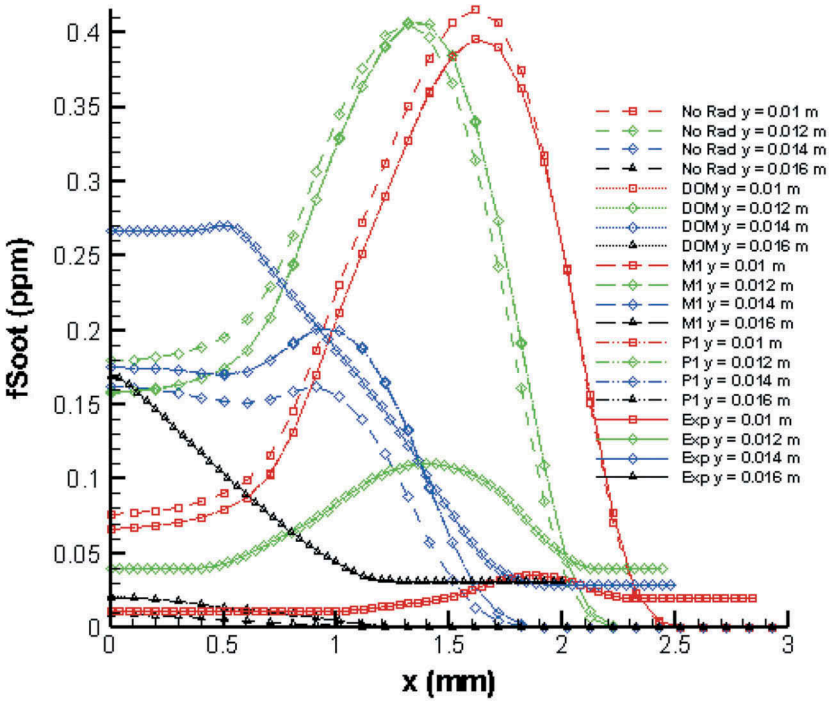

Figure 22. Radial profiles for soot volume fraction at different axial locations at 1 atm.

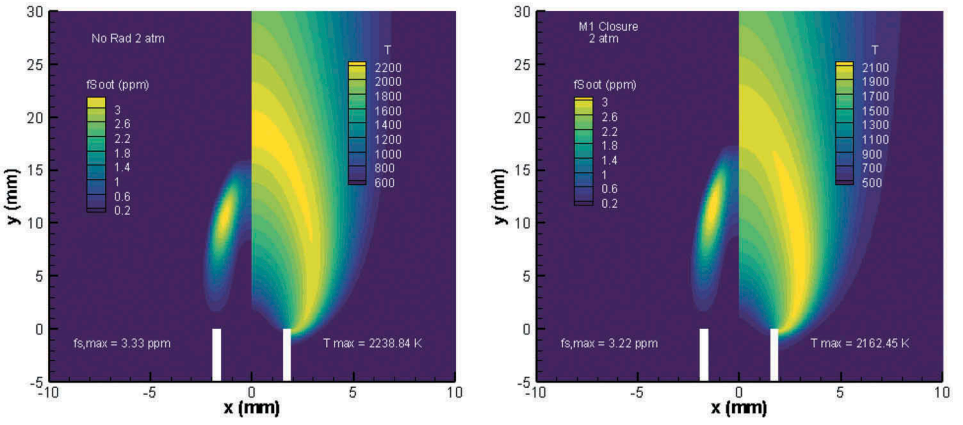

(a) Solution with no radiation (b) M_1 solution

Figure 23. Comparison of contours of temperature and soot volume fraction predicted by (a) the case where radiation is neglected (b) the M_1 closure for a mixture of methane and ethanol at 2 atm.

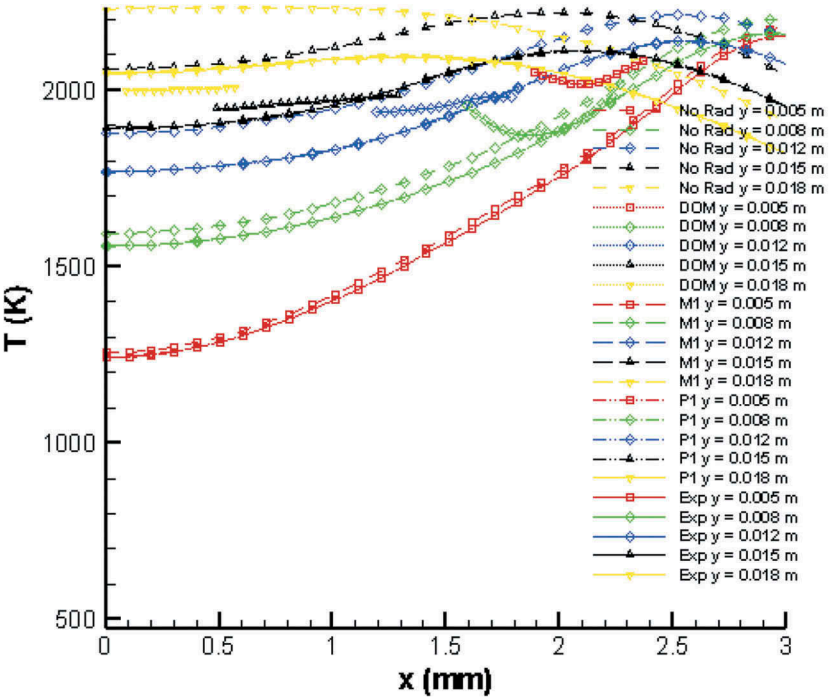

Figure 24. Radial profiles for temperature at different axial locations at 2 atm.

the M_1 moment closure. Furthermore, as should be expected, the numerical results obtained with radiative heat transfer afford significantly better predictions compared to those obtained without radiation, while the predictions of soot volume fraction and temperature obtained using the three different approximate models for radiative heat

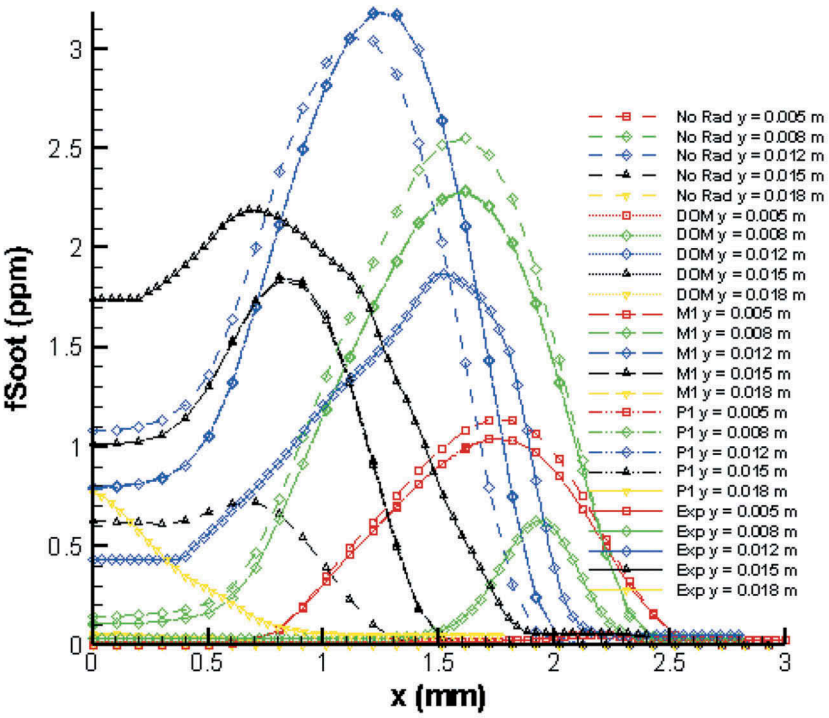

Figure 25. Radial profiles for soot volume fraction at different axial locations at 2 atm.

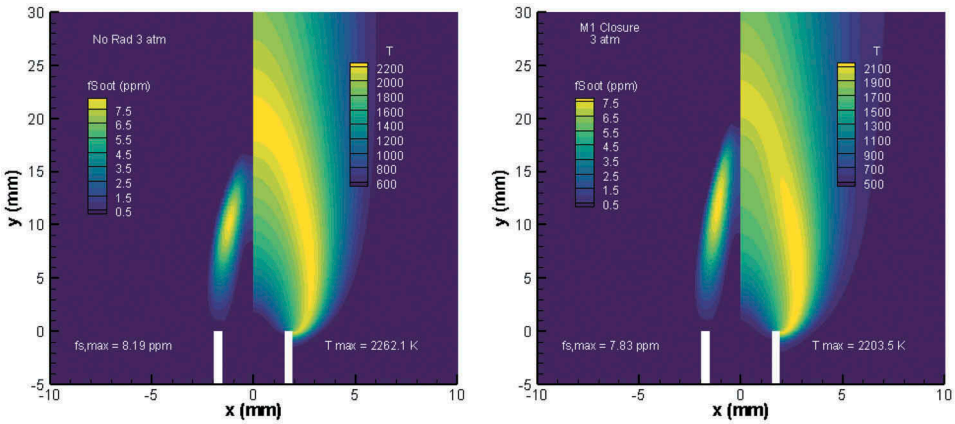

(a) Solution with no radiation (b) M_1 solution

Figure 26. Comparison of contours of temperature and soot volume fraction predicted by (a) the case where radiation is neglected (b) the M_1 closure for a mixture of methane and ethanol at 3 atm.

transfer considered here (M_1 and P_1 closures as well as DOM) are again in very good agreement with each other. The three radiation models again also all over-predict the values corresponding to the peak soot volume fraction closer to the burner rim and underpredict those quantities further downstream of the burner. At the lower flame

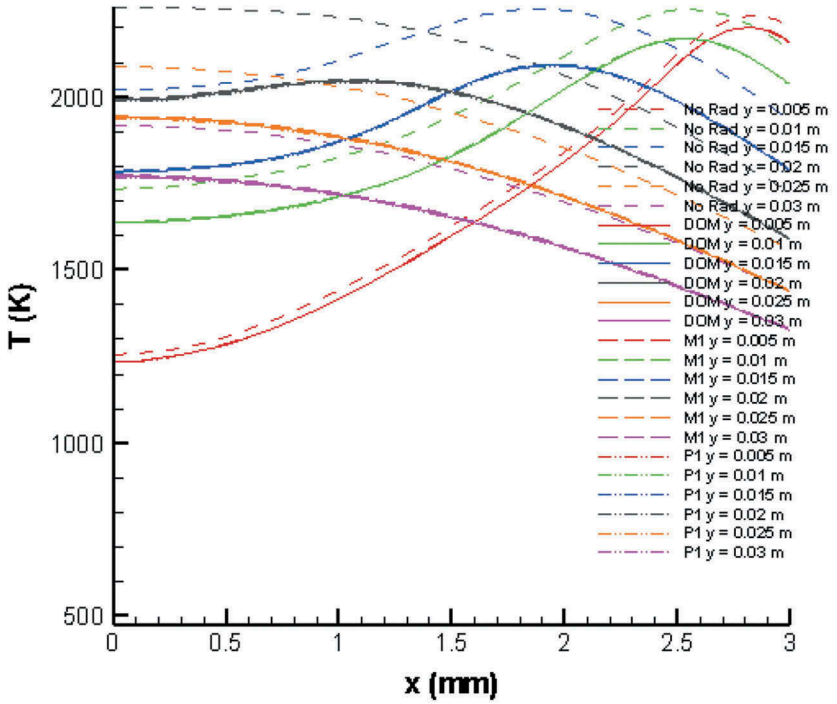

Figure 27. Radial profiles for temperature at different axial locations at 3 atm.

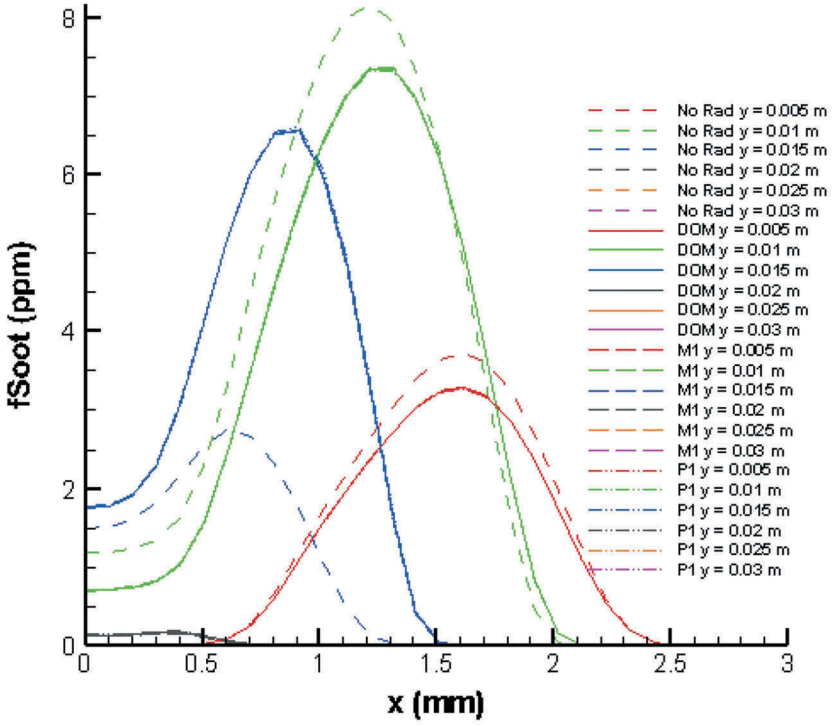

Figure 28. Radial profiles for soot volume fraction at different axial locations at 3 atm.

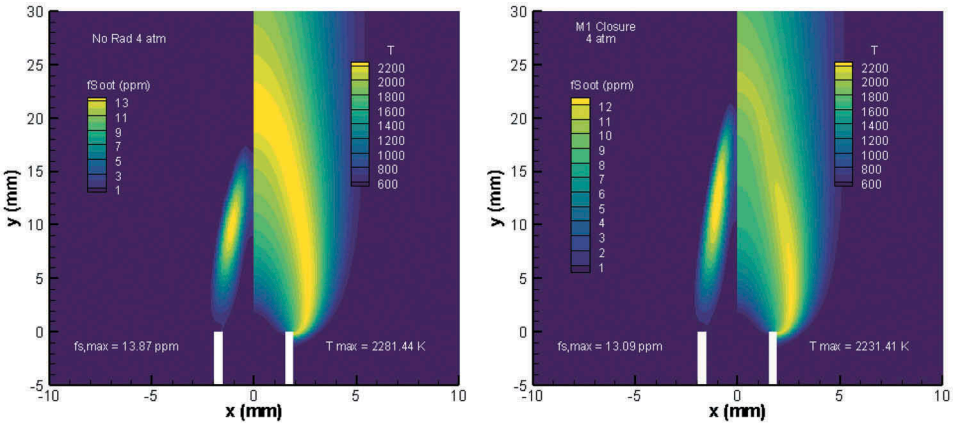

(a) Solution with no radiation (b) M_1 solution

Figure 29. Comparison of contours of temperature and soot volume fraction predicted by (a) the case where radiation is neglected (b) the M_1 closure for a mixture of methane and ethanol at 4 atm.

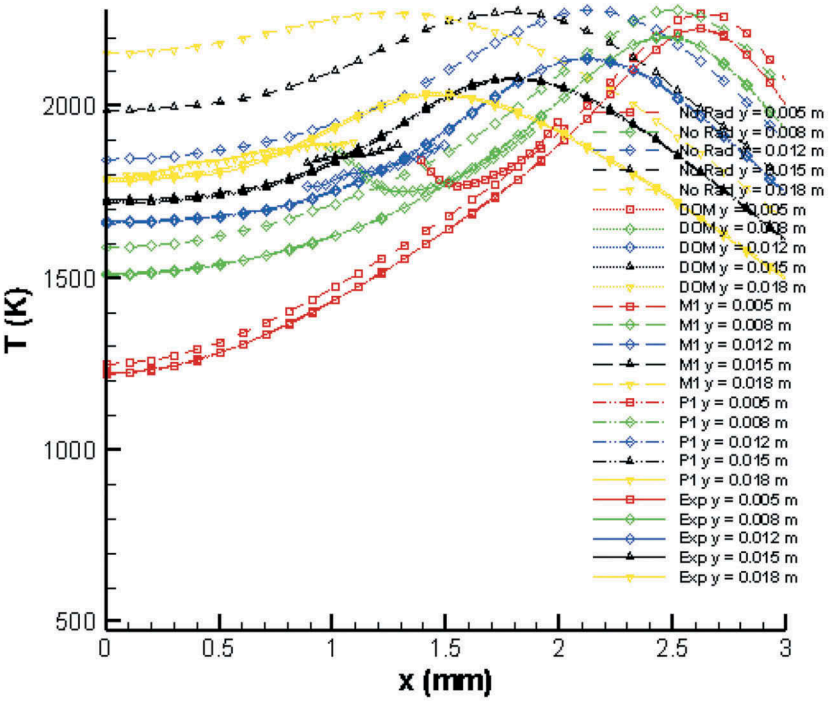

Figure 30. Radial profiles for temperature at different axial locations at 4 atm.

pressures, predictions of radial locations at which the peak soot concentrations occur are in good agreement with experimental data closer to the rim, while, at elevated pressures, the location of the peak is shifted radially-inward. In all cases, the location of the peak is shifted toward the centerline downstream of the burner.

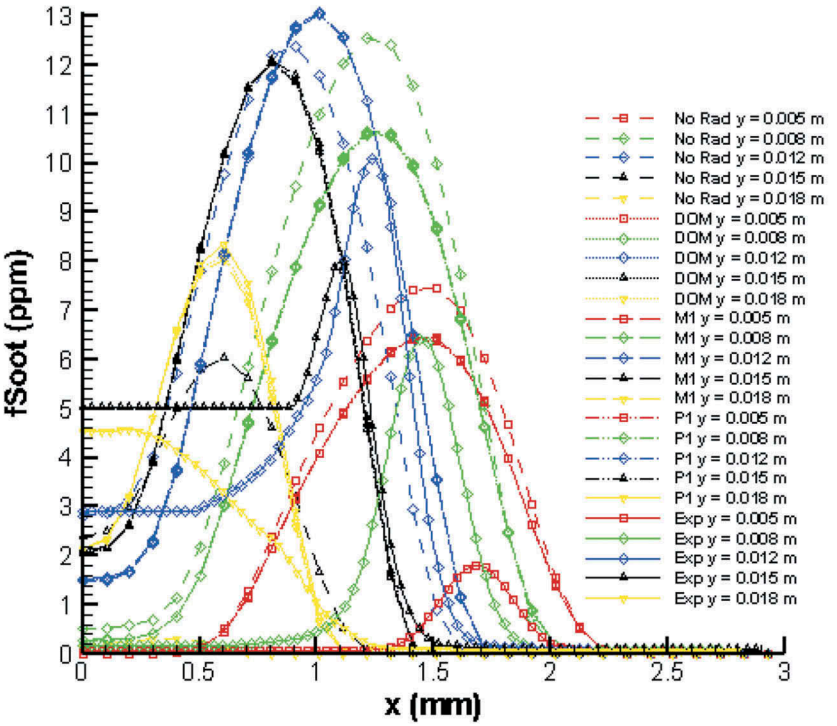

Figure 31. Radial profiles for soot volume fraction at different axial locations at 4 atm.

Conclusions

A new interpolative-based approximation of the non-gray first-order M_1 maximum-entropy moment closure for predicting radiative heat transfer in non-gray participating media has been developed. This newly developed analytical moment closure technique, in addition to accurately approximating pre-computed values obtained from the numerical solution of the optimization problem for entropy maximization, is also realizable and hyperbolic. Its predictive capabilities have been assessed by direct comparisons of its solutions of laminar diffusion flames simulations to those of the more popular first-order P_1 spherical harmonics moment closure and the discrete ordinates method, where the latter method was used as a benchmark for comparisons. Two families of laminar diffusion flames, in particular pure methane-air and ethanol-methane-air flames, were both considered. Steady-state numerical solutions of the moment equations for all cases considered were obtained using standard upwind finite-volume method with adaptive mesh refinement and a Newton Krylov–Schwarz iterative technique using a previously developed computational framework for laminar reactive flows with soot formation. For this relatively small, laboratory scale burner, both the non-gray M_1 and P_1 moment closures provided temperature and soot volume fraction solutions that were in very good agreement with each other and also with those obtained using the standard DOM. However, for more realistic, large scale geometries with relatively large optical thicknesses, which will be the subject of future studies, the newly developed non-gray M_1 closure would be expected to provide improved predictions and

additional computational robustness at the expense of only a rather modest increase in computational costs relative to the conventional P_1 closure. Furthermore, the total number of transport equations that must be solved is reduced by a factor of 14 in comparison to the two-dimensional DOM approach considered here. This reduction in the number of independent variables would make the newly developed M_1 closure a very good candidate for radiation calculations in reactive flows, especially in the context of turbulent flows with more realistic, complex geometries, where the space marching techniques generally used to solve the DOM equations would become rather inefficient. In such types of reactive flows, which will also be the subject of future follow-on studies, time averaging, or spatial filtering of the system of moment equations for the M_1 closure will result in an additional closure problem due to the nonlinearity of the Eddington tensor in terms of the lower-order moments. A special treatment of the latter will be required in order to obtain closed description of the radiative heat transfer. Development of interpolative approximations of higher-order maximum-entropy moment closures, in particular the second-order M_2 approximation in this hierarchy of closure techniques, will also be considered in future studies. Finally, implementation of the newly developed interpolative-based non-gray maximum entropy closures will be considered in the context of the full spectrum correlated-*k* (FSCK) model (Modest and Zhang 2002). The FSCK method is in fact expected to provide more efficient approximate radiation solvers since it solves directly for spectrally integrated quantities by directly reordering the spectral absorption coefficient into a monotonic function throughout the full spectrum, such that the total number of quadrature points required for integration over the full range of wavenumbers is reduced compared to the SNBCK approach adopted herein.

Acknowledgments

This research was funded by grants and contracts from the Green Aviation Research and Development Network (GARDN), Southern Ontario Smart Computing for Innovation Platform (SOSCIP), as well as Pratt & Whitney Canada. The first author also received support in the form of a scholarship from the Natural Sciences and Engineering Research Council (NSERC) of Canada. Additionally, the computational resources for performing the numerical simulations reported herein were provided by the SOSCIP program as well as the SciNet High Performance Computing Consortium at the University of Toronto and Compute/Calcul Canada (the latter are funded by the Canada Foundation for Innovation (CFI) and Province of Ontario, Canada).

References

Akih-Kumgeh, B. (2013, May). (Private correspondence)

Cernohorsky, J., and S. A. Bludman. 1994. Maximum entropy distribution and closure for bose-einstein and fermi-dirac radiation transport. *Astrophys. J.* 433:250. doi:10.1086/174640.

Charest, M. R., C. P.T. Groth, and Ö. L. Gülder. 2010. A computational framework for predicting laminar reactive flows with soot formation. *Combust. Theor. Model.* 14 (6):793–825. doi:10.1080/13647830.2010.512960.

Charest, M. R., C.P.T. Groth, and Ö. L. Gülder. 2011. Effects of gravity and pressure on laminar coflow methane–Air diffusion flames at pressures from 1 to 60 atmospheres. *Combust. Flame* 158 (5):860–75. doi:10.1016/j.combustflame.2011.01.019.

Charest, M. R., C. P.T. Groth, and Ö. L. Gülder. 2012. Solution of the equation of radiative transfer using a Newton-Krylov approach and adaptive mesh refinement. *J. Comput. Phys.* 231 (8):3023–40. doi:10.1016/j.jcp.2011.11.016.

Charest, M. R., H. I. Joo, Ö. L. Gülder, and C. P.T. Groth. 2011. Experimental and numerical study of soot formation in laminar ethylene diffusion flames at elevated pressures from 10 to 35 atm. *Proc. Combust. Inst.* 33 (1):549–57. doi:10.1016/j.proci.2010.07.054.

Charest, M. R., Ö. L.Gülder, and C.P.T. Groth. 2014. Numerical and experimental study of soot formation in laminar diffusion flames burning simulated biogas fuels at elevated pressures. *Combust. Flame* 161 (10):2678–91. doi:10.1016/j.combustflame.2014.04.012.

Dubroca, B., and J.-L. Feugeas. 1999. Theoretical and numerical study on a moment closure hierarchy for the radiative transfer equation. *SIAM J. Numer. Anal.* 329 (10):915–20.

Einfeldt, B. 1988. On Godunov-type methods for gas dynamics. *SIAM J. Numerial. Anal.* 25 (2):294–318. doi:10.1137/0725021.

Fairweather, M., W. P. Jones, and R. P. Lindstedt. 1992. Predictions of radiative transfer from a turbulent reacting jet in a cross-wind. *CF* 89:45–63.

Fiveland, W. A. 1984. Discrete-ordinates solutions of the radiative transport equation for rectangular enclosures. *J. Heat Transfer* 106 (4):699. doi:10.1115/1.3246741.

Gao, X., S. Northrup, and C.P. T. Groth. 2011. Parallel solution-adaptive method for two-dimensional non- premixed combusting flows. *PCFD* 11 (2):76. doi:10.1504/PCFD.2011.038834.

Godunov, S. K. 1959. A finite difference method for the computation of discontinuous solutions of the equations of fluid dynamics. *Mat. Sb.* 47:357–93.

Goutiere, V., A. Charette, and L. Kiss. 2002. Comparative performance of nongray gas modeling techniques. *Num HTB* 41 (3–4):361–81.

Grad, H. 1949. On the kinetic theory of rarefied gases. *Commun. Pure Appl. Math.* 2 (4):331–407. doi:10.1002/(ISSN)1097-0312.

Griffin, E. A., M. Christensen, and Ö. L. Gülder. 2018. Effect of ethanol addition on soot formation in laminar methane diffusion flames at pressures above atmospheric. *Combust. Flame* 193:306–12. doi:10.1016/j.combustflame.2018.04.001.

Groth, C. P. T., and S. A. Northrup (2005). Parallel implicit adaptive mesh refinement scheme for body-fitted multi-block mesh. *17th AIAA Computational Fluid Dynamics Conference*, Toronto, Ontario, Canada.

Guo, H., F. Liu, G. J. Smallwood, and Ö. L. Gülder. 2002. The flame preheating effect on numerical modelling of soot formation in a two-dimensional laminar ethylene-air diffusion flame. *CombTM* 6:173–87.

Gupta, A., M. F. Modest, and D. C. Haworth. 2009. Large-eddy simulation of turbulence-radiation inter- actions in a turbulent planar channel flow. *J. Heat Transfer* 131 (6):061704. doi:10.1115/1.3085875.

Harten, A. 1983. High resolution schemes for hyperbolic conservation laws. *J. Comput. Phys.* 49 (3):357–93. doi:10.1016/0021-9991(83)90136-5.

Hirschfelder, J. O., C. F. Curtiss, and R. B. Byrd. 1969. *Molecular theory of gases and liquids*. New York: John Wiley & Sons.

Jaynes, E. T. 1957. Information theory and staistical mechanics. *Phys. Rev.* 106:620–30. doi:10.1103/PhysRev.106.620.

Jeans, J. H. 1917. The equations of radiative transfer of energy. *Mon. Not. R. Astron. Soc.* 78 (1):28–36. doi:10.1093/mnras/78.1.28.

Joo, H. I., and Ö. L. Gülder. 2009. Soot formation and temperature field structure in co-flow laminar methane-air diffusion flames at pressures from 10 to 60 atm. *Proc. CI* 32 (1):769–75.

Kennedy, I. M., W. Kollmann, and J. Y. Chen. 1990. A model for the soot formation in a laminar diffusion flame. *CF* 81:73–85.

Kuo, K. K. 2005. *Principles of combustion*. 2nd ed. New Jersey: John Wiley & Sons, Inc.

Lacis, A. A., and V. Oinas. 1991. A description of the correlated k distribution method for modeling nongray gaseous absorption, thermal emission, and multiple scattering in vertically inhomogeneous atmospheres. *J. Geophys. Res.* 96 (D5):9027–63. doi:10.1029/90JD01945.

Lathrop, K. D., and B. G. Carlson (1965). *Discrete ordinates angular quadrature of the neutron transport equation* (Report No. LA-3186). Los Alamos Scientific Laboratory.

Leung, K. M., R. P. Lindstedt, and W. P. Jones. 1991. A simplified reaction mechanism for soot formation in nonpremixed flames. *CF* 87:289–305.

Levermore, C. 1984. Relating eddington factors to flux limiters. *J. Quant. Spectrosc. Radiat. Transfer* 31 (2):149–60. doi:10.1016/0022-4073(84)90112-2.

Li, G., and M. F. Modest. 2003. Importance of turbulence-radiation interactions in turbulent diffusion jet flames. *J. Heat Transfer* 125 (5):831. doi:10.1115/1.1597621.

Liu, F., G. J. Smallwood, and Ö. L. Gülder. 2000a. Application of the statistical narrow-band correlated- k method to low-resolution spectral intensity and radiative heat transfer calculations: Effects of the quadrature scheme. *Int. J. Heat Mass Transf.* 43 (17):3119–35. doi:10.1016/S0017-9310(99)00343-9.

Liu, F., G. J. Smallwood, and Ö. L. Gülder. 2000b. Band lumping strategy for radiation heat transfer calculations using a narrowband model. *JTHT* 14 (2):278–81.

Liu, F., H. Guo, G. J. Smallwood, and Ö. L. Gülder. 2002. Effects of gas and soot radiation on soot formation in a coflow laminar ethylene diffusion flame. *J. Quant. Spectrosc. Radiat. Transfer* 73:409–21. doi:10.1016/S0022-4073(01)00205-9.

Mazumder, S., and M. F. Modest. 1999. A probability density function approach to modeling turbulence- radiation interactions in nonluminous flames. *Int. J. Heat Mass Transf.* 42 (6):971–91. doi:10.1016/S0017-9310(98)00225-7.

Modest, M. F. 2013. *Radiative heat transfer*. 3rd ed. Academic Press.

Modest, M. F., and H. Zhang. 2002. The full-spectrum correlated-k distribution for thermal radiation from molecular gas-particulate mixtures. *J. Heat Transfer* 124 (1):30. doi:10.1115/1.1418697.

Modest, M. F., and R. S. Mehta. 2006. Modeling absorption tri in optically thick eddies. *Proc. Eurotherm78 - Computational Therm. Radiat. Participating Media II* 78:225–34.

Perera, F. P. 2016. Multiple threats to child health from fossil fuel combustion: Impacts of air pollution and climate change. *Environ. Health Perspect.* 125 (2). doi:10.1289/EHP36.

Pichard, T., G. W. Alldredge, S. Brull, B. Dubroca, and M. Frank. 2016. An approximation of the M2 closure: Application to radiotherapy dose simulation. *J. Sci. Comput* 71 (1):71–108.

Sachdev, J., C.P. T. Groth, and J. Gottlieb. 2005. A parallel solution-adaptive scheme for multi-phase core flows in solid propellant rocket motors. *Int. J. Comut. Fluid. Dyn.* 19 (2):159–77. doi:10.1080/10618560410001729135.

Sarr, J. A. R., C. P. T. Groth, and J. H. Hu (2019, October). A maximum entropy-inspired interpolative closures for the prediction of radiative heat transfer in non-gray participating media. submitted to the Journal of Quantitative Spectroscopy and Radiative Heat Transfer.

Smooke, M.D., C.S. McEnally, L.D. Pfefferle, R.J. Hall, and M. B. Colket. 1999. Computational and experimental study of soot formation in a coflow, laminar diffusion flame. *CF* 117:117–39.

Soufiani, A., and J. Taine. 1997. High temperature gas radiative property parameters of statistical narrow- band model for H2O, CO2 and CO, and correlated-k model for H2O and CO2. *Int. J. Heat Mass Transf.* 40 (4):987–91. doi:10.1016/0017-9310(96)00129-9.

Thurgood, C. P., A. Pollard, and H. A. Becker. 1995. TN quadrature set for the discrete ordinates method. *JHT* 117 (4):1068–70.

Turpault, R. 2002. Construction of a multigroup m1 model for the radiative transfer equations. *C. R. Acad. Sci. Paris, Ser. I* 334:331–36. doi:10.1016/S1631-073X(02)02265-3.

Turpault, R. 2005. A consistent multigroup model for radiative transfer and its underlying mean opacities. *J. Quant. Spectrosc. Radiat. Transfer* 94 (3–4):357–71. doi:10.1016/j.jqsrt.2004.09.042.

Viskanta, R., and M. P. Mengüç. 1987. Radiation heat transfer in combustion systems. *Prog. ECS* 13:97–160.